Evaluation of Phase Change Material Thermal Control Architectures for a WaferSatellite using Integrated Design and Optimization Techniques

by

Michael G. Fifield

B.S., Georgia Institute of Technology (2015)

Submitted to the Department of Aeronautics and Astronautics
in partial fulfillment of the requirements for the degree of

Master of Science

at the

MASSACHUSETTS INSTITUTE OF TECHNOLOGY

June 2019

Author ..... Signature redacted
Department of Aeronautics and Astronautics
May 24, 2019

Certified by ..... Signature redacted .....
David W. Miller
Professor of Aeronautics and Astronautics
Thesis Supervisor

Certified by ..... Signature redacted .....
Rebecca A. Masterson
Principal Research Scientist
Thesis Supervisor

Accepted by ..... Signature redacted ..
Sertac Karaman
Associate Professor of Aeronautics and Astronautics
Chair, Graduate Program Committee

Evaluation of Phase Change Material Thermal Control Architectures for a WaferSatellite using Integrated Design and Optimization Techniques

by

Michael G. Fifield

Submitted to the Department of Aeronautics and Astronautics
on May 24, 2019, in partial fulfillment of the
requirements for the degree of
Master of Science

Abstract

Small satellites such as CubeSats are changing the satellite industry by offering low-cost access to space. The concept of WaferSat – a satellite consisting of only a single silicon wafer – seeks to take this paradigm one step further, utilizing microelectromechanical systems processes to reliably enable mass-producible spacecraft with the potential to form large space sensor arrays. However, as a 200 mm diameter silicon wafer with only 250 grams of mass, WaferSat has little heat capacity. Therefore, temperatures on the spacecraft rapidly approach extremes in eclipse and sunlight. Moreover, the highly integrated nature of WaferSat couples the thermal design challenge to other subsystems.

This thesis seeks to explore the potential application of phase change materials to efficiently increase effective heat capacity to reduce the temperature extremes attained on-orbit. An integrated design and optimization framework is utilized to optimize the selection of phase change materials and masses in the presence of severe system resource constraints. Two reference mission scenarios are explored. First, a minimum mass solution is obtained for a fixed-attitude case. Next, a scenario of varied WaferSat attitudes is shown to reduce the required phase change material mass. Finally, design implications and future work to improve implementation feasibility are presented.

Thesis Supervisor: David W. Miller
Title: Professor of Aeronautics and Astronautics

Thesis Supervisor: Rebecca A. Masterson
Title: Principal Research Scientist

Acknowledgments

This work was funded through the WaferSat project by MIT Lincoln Laboratory, contract #7000389700. I would like to express my gratitude to all of the Lincoln Laboratory staff involved in the WaferSat project.

I would like to thank Professor Dave Miller and Dr. Rebecca Masterson for their advising and insights which helped shape and guide the work in this thesis. I would also like to acknowledge all of my labmates in the SSL and give a special thanks to Dr. Mark Chodas for his willingness to help and provide technical assistance in the eleventh hour.

Finally, a big thank you to Mom, Dad, and my sister, Jennifer, for all of their love and unwavering support every step of the way.

Contents

List of Figures

List of Tables

List of Abbreviations

AI&T	Assembly, Integration, and Test
CONOPS	Concept of Operations
MDO	Multi-disciplinary Optimization
MEMS	Microelectromechanical Systems
PCB	Printed Circuit Board
PCM	Phase Change Material
SWaP	Size, Weight, and Power
SWaP-C	Size, Weight, and Power, and Cost
TCS	Thermal Control System
WaferSat	Wafer Satellite

List of Symbols

γ	Attitude angle from Wafer top side normal to Earth-Sun vector
σ	Steffan-Boltzmann constant
θ	True anomaly, referenced to Earth-Sun vector
α_*	Absorptivity, visible light wavelengths
ε_*	Emisivity, infrared wavelengths
ϕ_{SA}	Solar array physical fill factor
$(\cdot)_{B-E}$	Wafer bottom surface to Earth
$(\cdot)_{B-S}$	Wafer bottom surface to Sun
$(\cdot)_{T-E}$	Wafer top surface to Earth
$(\cdot)_{T-S}$	Wafer top surface to Sun
A_E	Mean Earth albedo
C_p	Specific heat capacity at constant pressure
E_{sol}	Solar irradiance flux density at 1 AU
H_t°	Latent heat of phase transition
I_E	Mean Earth IR flux density
L_{frac}	PCM liquid fraction by mass
Q_{A-B}	Earth-reflected solar irradiance incident upon Wafer bottom surface
Q_{A-SA}	Earth-reflected solar irradiance incident upon solar array
Q_{A-T}	Earth-reflected solar irradiance incident upon Wafer top surface
Q_{I-B}	Earth IR incident upon Wafer bottom surface
Q_{I-SA}	Earth IR incident upon solar array
Q_{I-T}	Earth IR incident upon Wafer top surface

Q_{S-B}	Solar irradiance incident upon Wafer bottom surface
Q_{S-SA}	Solar irradiance incident upon solar array
Q_{S-T}	Solar irradiance incident upon Wafer top surface
Q_{int}	WaferSat continuous internal heat dissipation
R_E	Radius of the Earth
h	WaferSat orbit altitude

Chapter 1

Introduction

1.1 Motivation

Satellite development is an inherently complex process. The demanding environment of space necessitates a multidisciplinary approach wherein the considerations of all subsystems must coalesce into an integrated system. From a high level, spacecraft complexity can be expressed as size, weight, and power as well as cost (SWaP-C). Conventional satellite design tends towards higher SWaP-C systems to efficiently enable high capability (e.g., many hosted payloads, high power provided to payloads, etc.). However, such systems can be prohibitively costly to develop and field. Furthermore, the relatively long development timescales limit the rate of upgrade.

To combat the design challenges associated with large spacecraft, recent trends in spacecraft design have focused on small satellites, specifically those 10 kg and lower. The standard convention defining small satellites is as follows: nanosatellites ranging from 1 to 10 kg, picosatellites from 0.1 to 1 kg, and femtosatellites less than 0.1 kg. Small satellites benefit from reduced cost-to-orbit by virtue of their lower mass. The reduction in complexity also shortens the development time-scale.

The combination of lower cost and relatively short development timeline significantly increase opportunities for access to space. The low unit-cost can enable launches of multiple units to efficiently create large distributed or fractionated sensor networks.

However, these advantages come at a cost; the reduction in SWaP-C limits capability. As a result, small satellites typically host smaller, simpler payloads. The emergence of the cubesat platform in the nanosatellite class has provided a standardized and accessible small satellite bus. Despite the reduction in size, weight, and power, surveys of recent cubesat missions have shown a marked shifted in focus from pedagogical objectives to scientific data gathering, demonstrating that the cubesat platform is able to support capable payloads [8, 9].

Smaller still are the concepts for satellites-on-a-chip ranging from less than 10 grams to several hundred grams. Such systems seek to benefit from the developments from the Microelectromechanical Systems (MEMS) production techniques developed for and utilized by the electronics industry. Today, MEMS industry production offers high-yield, high-volume, limited touch-labor production of chips and integrated circuits. Concepts for satellites-on-a-chip seek to bring this efficient method of production to satellites.

Consideration of several small satellite scales engenders several questions regarding the balance of capability, SWaP budgets, and Assembly, Integration, and Test (AI&T) complexity. Specifically, is there a scale that balances the benefits from minimal touch-labor AI&T, low mass/volume, and provides sufficient resources for capable payloads? At this scale, do traditional spacecraft design solutions satisfy requirements under more severe resource constraints?

A 150-300 gram, 200 mm diameter, single MEMS silicon wafer satellite (WaferSat) may reap the benefits of scale whilst maintaining sufficient SWaP to enable a number of high-functioning payloads. Whereas CubeSats often approach subsystem design in a modular fashion with clear delineation between subsystems, the more

highly integrated nature of WaferSat necessitates a similarly more integrated design approach. The SWaP limitations place new constraints on the design space that now must be efficiently navigated with multidisciplinary consideration. The limits on mass, volume/form factor, and adjacency of components necessitates that elements become multi-use, blurring the distinction between subsystems.

Of particular concern is consideration of thermal control and maintenance. At several hundred grams of total mass, there is little thermal inertia, resulting in large temperature extremes with short equilibration time constants. Many traditional thermal control architectures are too large or consume considerable amounts of system resources such as power. Phase change material heat storage may offer increased thermal inertia with low resource consumption as a passive solution (that may stand alone, or augment another active or passive system). This thesis seeks to evaluate the feasibility of a phase change material heat-storage thermal control architecture for a WaferSat using an integrated design approach.

1.2 Literature Review

This research will combine elements of design from three areas: small satellite design, integrated design optimization methods, and satellite thermal control architectures. The work in this thesis resides at the intersection of these three areas and is subject to the constraints set by the MEMS scale.

1.2.1 Small Satellite Design

Recent years have seen a rapid growth in the number of CubeSat missions. Originally conceived of as a platform to provide students with an opportunity to develop flight spacecraft, the CubeSat standard provides a unified platform for small satel-

lite development at low development, fabrication, and launch cost [10]. The rapid emergence and growth has spurred development of modular subsystem components. The standardization of subsystem interfaces within the platform has enabled work on automated design in 'Plug-and-Play' fashion [11]. This approach offers a foreshortened development process by encapsulating spacecraft subsystems with standardized interfaces to ensure compatibility.

At the forefront of small satellite development are even smaller picosats and femtosats. Ranging from the tens to hundreds of grams, such satellites may consist of only a single Printed Circuit Board (PCB) or silicon wafer (effectively a monolithic integrated circuit satellite). The concept of a satellite-on-a-chip was proposed as early as 1994 [12]. In 2000, two tethered, sub-300 gram PicoSats, developed by the Aerospace Corporation were deployed by the Orbiting Picosatellite Automated Launcher (OPAL) [13]. The two PicoSats demonstrated operation of MEMS radio frequency switches for low power crosslink communication across the tether. Interestingly, the system architecture would ultimately grow in size to inform the development of the CubeSat standard. Concept studies and analysis continued for satellites-on-a-chip using a silicon wafer substrate [14], though none were produced and launched as a follow-on to this program.

Further improvements to MEMS process yield and reliability [15] indicate viability of efficient, large scale production to create large constellations of satellites. Work by Barnhart et al. on Satellite-on-a-chip concepts explores the benefits of low unit cost and potential for application in large, distributed sensor networks [1, 16]. Barnhart's study advanced the concept for a satellite-on-a-chip, addressing feasibility in SWaP, downlink communications, crosslink, and distributed payload applications. A simple concept of a 'SpaceChip' is shown in Figure 1-1 with rough subsystem size estimates.

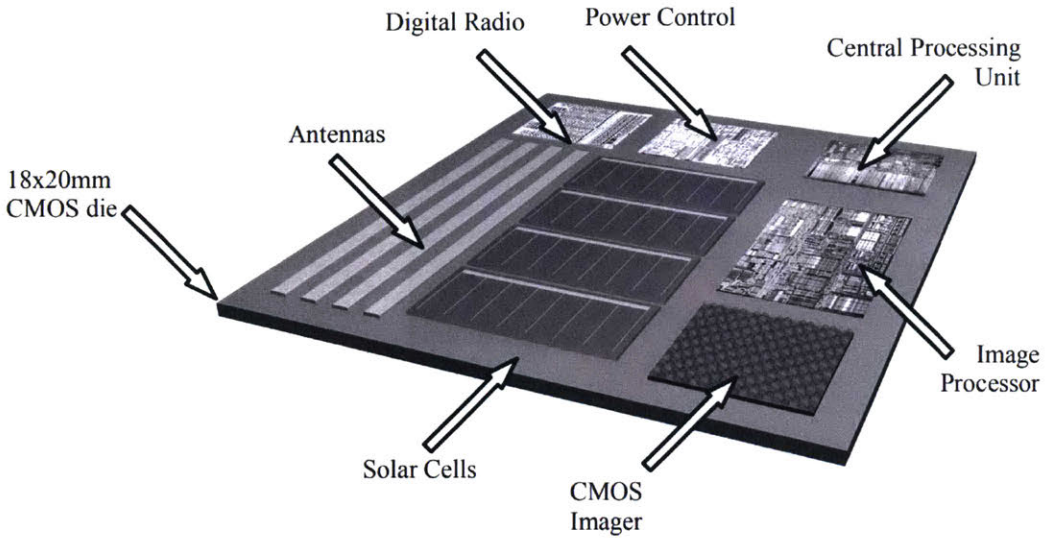

Figure 1-1: A Proposed Satellite-on-a-Chip, SpaceChip [1]

More recently, there has been renewed interest in the satellite-on-a-chip concept at the femtosat scale to enable deep space exploration. The Breakthrough Starshot initiative proposes to accelerate swarms of 1 g chipsats to 20% of the speed of light to eventually reach Alpha Centauri [17]. In 2013 KickSat, the first KickStarter-funded satellite, a 3U CubeSat carrying 120 5-gram chipsats launched [2]. Although the 'Sprite' chipsats did not successfully deploy, a second mission, KickSat-2 was launched in 2019. The Sprite chipsats – shown in Figure 1-2 – each consisted of a single 3.5 mm by 3.5 mm PCB with solar cells, MEMS gyro and magnetometer, and a UHF radio with omnidirectional antennas. In March of 2019, the Sprite chipsats were successfully deployed and established downlink to several ground-station receivers, demonstrating orbit-to-ground link budget closure from a chipsat [18]. Work by Lubin et al. also focuses on development of WaferSats at the sub-10 gram scale (femtosat-scale) to enable relativistic flight for deep space travel [19]. However the prior examples of sub-10 gram systems offer limited capability to support a dedicated payload. Work in this thesis is centered around the development towards a WaferSat in the hundreds of grams (picosat-scale) with a focus on maximizing potential capability to carry a scientific payload.

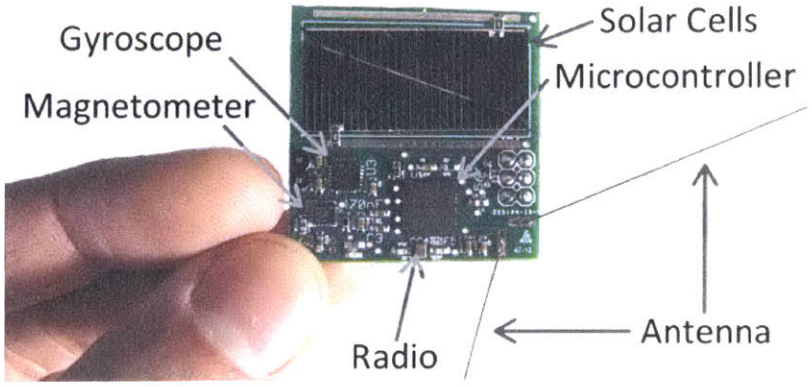

Figure 1-2: KickSat Project 5-gram "Sprite" chipsat [2]

Though the previous flight examples of ChipSats have been relatively simple in capability, feasibility studies by Barnhart et al. highlight the many challenges facing scientific payload-carrying ChipSats and WaferSats which include payload mass fraction allocation, electrical power system sizing and functionality at scale, and thermal control [20]. To address these challenges within the tight constraints, an integrated approach is required.

1.2.2 Traditional Satellite Thermal Control Architectures

The primary objective of the thermal control subsystem of any spacecraft is to maintain the temperatures of all subsystem components within their respective operational and survival ranges. At its core, this objective refers to management of thermal energy of the spacecraft, including rates of heat absorption and emission, internal energy dissipation, and heat storage. Thermal control can be separated into two main categories: active and passive control. Table 1.1 below shows the active and passive thermal control architectures commonly used on spacecraft.

Table 1.1: Active and Passive Spacecraft Thermal Control Techniques

Passive Control	**Active Control**
radiator	heaters
surface finish	thermoelectric cooling
MLI	cryocooler pumps
louvers	fluid loop
heat storage	electrochromics
heat pipes	view factor control
isolation	
coupling	
ablation	
thermochromics	

A traditional approach to thermal subsystem design is outlined in SMAD [3] as shown in Figure 1-3. First, thermal ranges and constraints are applied based on subsystem requirements. Then, thermal environments are defined based on the operational scenarios. These environments are typically conservatively constructed to offer significant margin to the system. Using the the thermal requirements and thermal environmental scenarios, the most limiting 'problem areas' that will need intervention are identified. To meet requirements in these problem areas, suitable thermal control architectures (selected from known techniques as in Table 1.1 above) are selected and analyzed. The radiators and heaters are sized and the overall thermal control system (TCS) mass and power are conservatively estimated. Throughout the design, this process is iterated to meet all requirements.

However, the conventional approach relies on system margin and gives little consideration to optimization of the thermal design. Instead, the approach makes the assumption that thermal subsystem design is not a driver of mission performance. A thermal path design optimization method proposed by Stout identifies four key cases

where traditional thermal control system (TCS) design approaches are inefficient or inadequate [21]. These include systems where:

a.) TCS performance is tightly linked to mission performance

b.) The TCS is closely physically linked to other subsystems

c.) The thermal challenges facing the system are significant to overcome

d.) The system is extremely resource-constrained

In the case of WaferSat, scenarios b, c, and d all apply (scenario a may also apply, depending on payload/mission application). As a single chip with little mass and volume, all elements and subsystems are closely linked thermally. Co-location and adjacency define a thermally coupled system where isolation is extremely challenging. The flat, thin form factor creates large absorptive and emissive surfaces giving rise to extreme hot and cold conditions. With low intrinsic thermal storage capability due to low mass, these temperature extremes are attained with short time constants. Therefore, consideration of TCS as a design driver is required for WaferSat; TCS design must occur concurrently with design of other subsystems to meet all requirements in such a constrained design-space. The hypothesis of this thesis is that a robust thermal control architecture with low system resource impact will combine heat storage, surface finish control, and attitude control to alter radiating view factors.

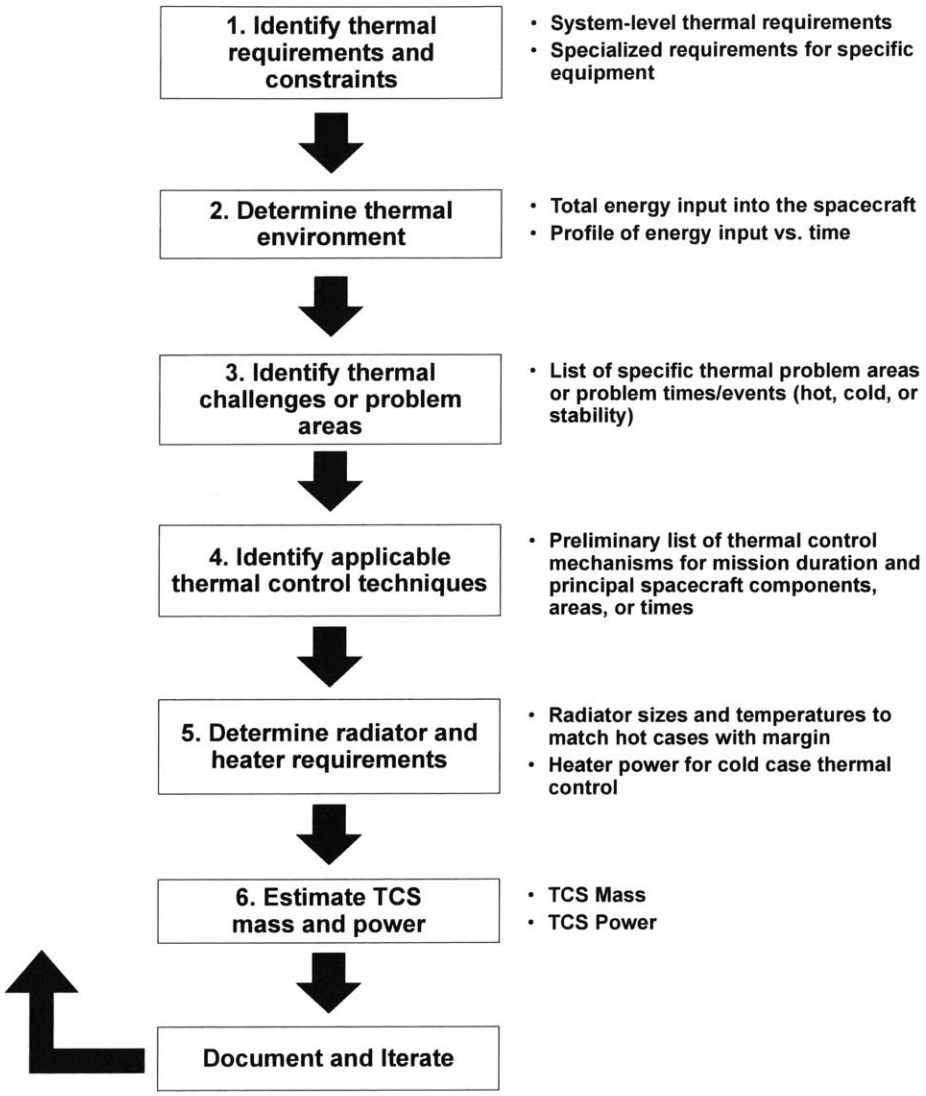

Figure 1-3: Traditional Spacecraft Thermal Design Process (SMAD) [3]

1.2.3 Phase Change Materials

One method to address the challenge of limited thermal inertia on WaferSat is to increase heat storage capacity, thereby slowing the rates of thermal equilibration. Phase change materials (PCM), which store heat at constant temperature during a phase transition, offer a high-density form of energy storage.

There are several historical examples of PCM usage in the space environment dating back to the Apollo program. The Lunar Rover Vehicle carried two boxes of paraffin wax to sink heat away from the batteries and drive electronics [22], offering a more compact solution than a radiator. The Soviet Venera probes 8, 9, and 10, which were sent to Venus orbit, carried lithium nitrate trihydrate to weather the extreme thermal environment. The enhanced heat storage afforded by the PCM extended the mission lifetime of the landers, allowing Venera-13 to survive on the surface of Venus for 117 minutes at temperatures of 457 °C [23]. In 1998, STS-95 included a Cryogenic Thermal Storage Unit (CRYOTSU) experiment which utilized cryocoolers. Due to the internal heat dissipation of the cryocoolers (which cannot be rejected from the system fast enough), the experiment required duty cycling. Inclusion of a 600 W Hr capacity phase change material compartment – shown in Figure 1-4 – to store rejected heat enabled extension of the operating duty cycle phase [24]. The embedded PCM compartment was utilized in conjunction with heat pipes to create a high heat capacity, isothermal radiator.

More recently, there have also been several studies that have analyzed potential implementations on spacecraft. Analysis by Collette, et al., (2011), performed analysis of an organic solid-liquid PCM as a means to reduce required radiator size of an Earth-orbiting satellite [25]. Their study showed potential mass savings in the trade of added PCM mass versus radiator size. Furthermore, scaling analysis suggested possible active thermal control power savings as overall system mass decreases.

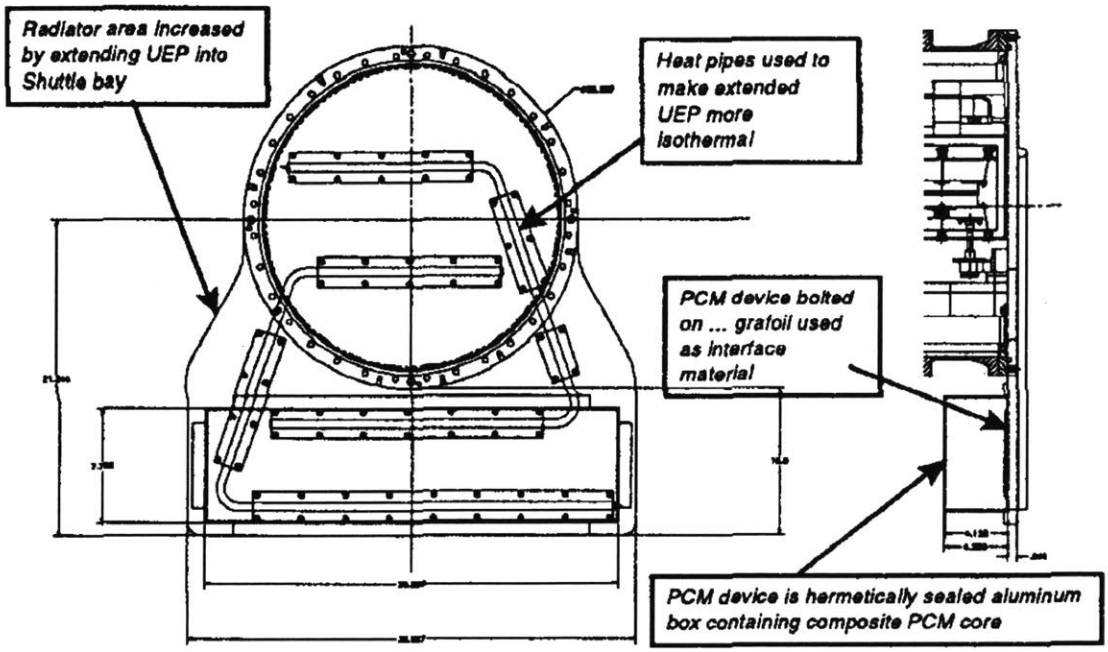

Figure 1-4: CRYOTSU PCM Upper Radiator End Plate [4]

1.2.4 Integrated Design Methods and Optimization

The extreme environment on orbit levies many constraints on the available design space. As such, subsystems must compete for resources such as mass and power. This challenge is exacerbated by reductions in spacecraft SWaP when designing at small-scale, thereby creating a need for economization and optimization of resource allocation. The decreased SWaP also further necessitates an approach that simultaneously considers the many subsystem interactions and constraints. Much work has been performed in the areas of integrated design and multidisciplinary optimization for spacecraft.

Work by Jilla developed a methodology to formulate distributed satellite system design as mathematical optimization problems [26, 27, 28]. In this approach, the conceptual design is defined by a decision vector containing the key design parameters. Constraints are applied and optimization objectives such as maximization of system performance, minimization of system cost, maximization of reliability are

applied. Combined modeling of subsystems allows for multi-disciplinary evaluation of performance.

In spacecraft design, the optimization landscape often boils down to tradeoffs among performance, cost, risk, and schedule. Noting this, de Weck presented an isoperformance approach to optimization in which performance invariant solutions are identified [29, 30]. By working 'backwards' from the desired performance objectives, performance invariant contours that meet these objectives are searched. This enables identification of minimum cost or risk options that achieve the desired performance targets.

Martins and Lambe (2013) provide a survey of multi-disciplinary optimization (MDO) methods [31]. In it, they explore several architectures, particularly those that are based upon the Extended Design Structure Matrix [5]. Subsystems are organized in a matrix with connective elements, transferring parameters as inputs and outputs. One such method, the Gauss-Seidel analysis process, is shown in Figure 1-5. Design vector x and the response variables y, enable concurrent modeling and evaluation of the multiple disciplines.

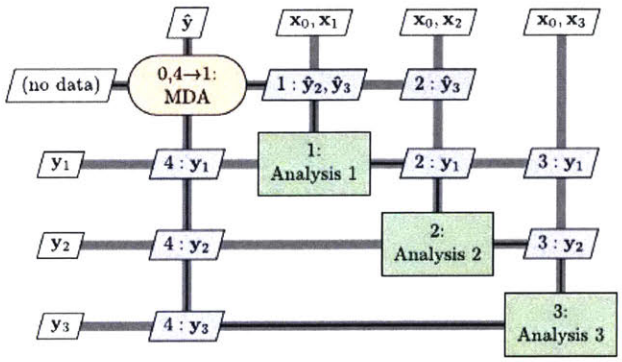

Figure 1-5: 3-Element Gauss-Seidel Multi-disciplinary Analysis [5]

Optimization techniques have similarly been applied to thermal subsystem design for spacecraft. Research by Stout on thermal path optimization poses thermal subsystem design space in the context of system resource consumption and overall system

performance [21]. Stout notes that the traditional design process assumes that the thermal subsystem is not a key determinant of system performance, nor a significant consumer of resources. Thus, late commencement of the thermal design results in a design that is designed in relative isolation, with limited consideration of the design space. His approach utilizes parametric modeling with subsystem interactions to ensure that the full design space is explored.

1.3 Research Objective

At the center of the design challenge for WaferSat is a set of constraints brought about by the MEMS scale. In particular, the mass and volume constraints severely restrict the available system resources and limit many of the traditionally utilized thermal control architectures. Of particular concern is the low thermal mass, that results in large temperature extremes on-orbit. The nature of the low mass system is strongly at odds with the traditional modularized design approach that allows for relative separation of subsystems. Co-location and interconnectedness which drive architectural design decisions also simultaneously limit traditional design options. The search for an architecture that satisfies thermal requirements while maximizing overall system capability requires decision-making in a highly multi-disciplinary context. The close adjacency of subsystems removes the clear delineations that are present on larger spacecraft and so the thermal subsystem must satisfy the thermal requirements whilst limiting consumption of the scarce, shared system resources.

The objective of this thesis is as follows:

To examine feasibility and performance of phase change material thermal design architectures at the MEMS-scale for a WaferSatellite

By evaluating system temperature stability and mass impact under defined mission scenarios

Using an integrated design and optimization approach

1.4 Thesis Roadmap

This thesis is organized into five parts. In Chapter 1 the motivation and thermal design challenge of WaferSat are established. An overview of past research in the areas of small satellite design, integrated optimization, and thermal subsystem design is presented. The intersection of these three areas, subject to the constraints levied by MEMS-scale production defines the area of research.

In Chapter 2, an overview of latent heat storage is given and a survey of the implementation and use of phase change materials assists in establishment of the design space.

In Chapter 3, an outline of the approach to the integrated design and evaluation of PCM architectures is presented. The mathematical frameworks of the subsystem models are defined and the optimization scheme and objectives are introduced in the context of architectural evaluation. In Chapter 4, an example of PCM operation is constructed to illustrate the distinct PCM operating regimes.

In Chapter 5 the optimization problem is presented in the context of WaferSat, setting the requirements and modeling assumptions. The results of the analysis in the framework established in chapter 3 are presented for a Sun-facing scenario and a thermally-favorable attitude profile. Conclusions and implications for design with PCMs are discussed.

A summary of the the conclusions that can be drawn from this research is given in Chapter 6, providing conclusions for application the WaferSat thermal control system. A path forward is offered for potential future research directions to expand upon the work of this thesis.

Chapter 2

Background

2.1 Phase Change Materials

2.1.1 Sensible and Latent Heat

Temperature can be defined as the thermal energy contained in a body. As thermal energy is added to a body as heat, the temperature rises according to equation 2.1. ΔQ, the heat added, is equal to the integral of the product of the mass of the object, m, the specific heat capacity, c_p, and dT from an initial temperature T_0 to a final temperature, T_f. The specific heat capacity is a function of temperature. If c_p is assumed to be constant – typically accepted over small temperature ranges – equation 2.1 simplifies to 2.2 where ΔQ, is equal to the product of the mass of the object, m, the specific heat capacity, c_p, and the change in temperature, ΔT.

$$\Delta Q = \int_{T_0}^{T_f} m c_p dT \tag{2.1}$$

$$\Delta Q = m c_p \Delta T \tag{2.2}$$

The storage of heat given in equations 2.1 and 2.2 refer to sensible heat storage; that is, heat storage that is *sensed* through a change in temperature. In this type of heat storage, the rise in temperature is governed by specific heat capacity – material property – and mass. Thus, for a given material, to increase total heat storage, mass must increase.

However, not all heat added to an object manifests as a rise in temperature. When a material undergoes a phase transition – e.g., melting from solid to liquid – thermal energy is absorbed at constant temperature. The absorbed heat is utilized in the phase change itself, expended during the melting process. This latent heat can be an effective method of heat storage to limit temperature change since the process is reversible. Energy absorbed in one direction – e.g., absorbed latent heat during melting – is released again in the reverse direction – e.g., emitted latent heat during freezing.

The total energy storage of both sensible and latent forms is expressed in equation 2.3 for an increase in temperature from T_0 to T_f, through the transition temperature, T_0, where $T_0 < T_t < T_f$. Terms 1 and 3 represent the sensible heat storage for temperature changes below and above T_t, as given by equation 2.1. Term 2, the latent heat term is the product of the specific latent heat capacity, H_t°, and the mass of the PCM, m.

$$\Delta Q = \int_{T_0}^{T_t} mc_p dT + mH_t^\circ + \int_{T_t}^{T_f} mc_p dT \tag{2.3}$$

The result is also shown pictorially in Figure 2-1 for a solid-liquid phase transition in the forward and reverse (endothermic and exothermic) directions. During the sensible temperature heat storage portions, the temperature varies linearly (assuming a uniform heat transfer rate in time). During the phase transition, there is a delay in the temperature change during heating and cooling, effectively increasing the heating and cooling time constants. The increase in time constant can be particularly useful in

the event that the heating and cooling phases are strictly time-limited. A significant delay in heating or cooling time constant will decrease the extent of the temperature extremes attained.

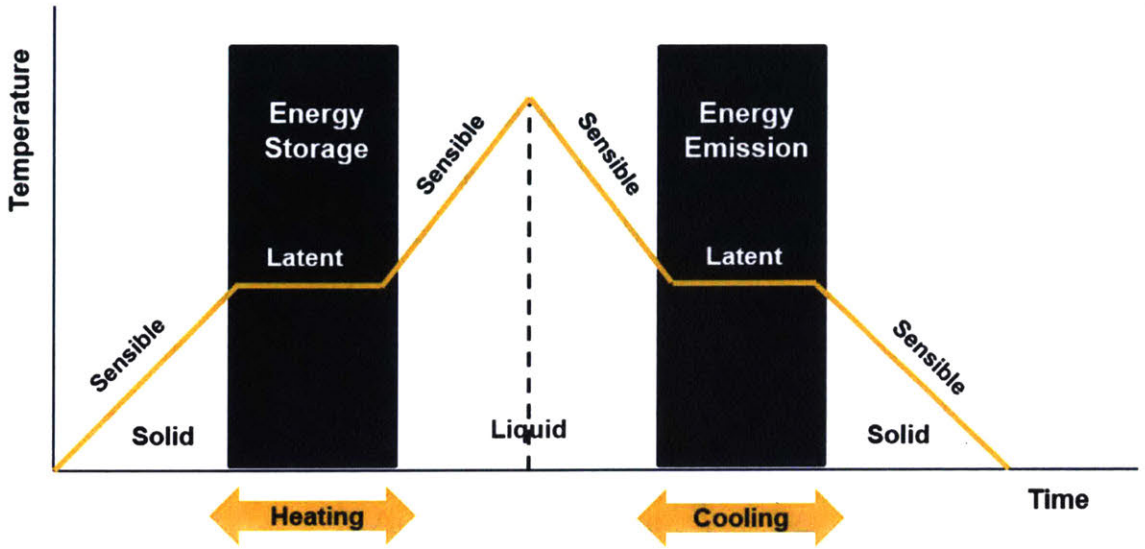

Figure 2-1: Example Heating and Cooling through Solid-Liquid Phase Transition [6]

2.1.2 PCM Usage

Usage of phase change materials, particularly in terrestrial applications, varies from the banal to the exotic. Perhaps the simplest and most ubiquitous example of the application of phase change heat storage is ice cubes in a glass of water. Ice cubes serve to maintain the temperature of the liquid near the freezing/melting point of water. As heat from the surrounding environment is absorbed by the water and ice cube mixture, the ice cubes melt, absorbing latent heat and maintaining the temperature. The process is reversible; if heat can be extracted, the water can be refrozen. This simple example highlights an important element of energy absorption during the phase transition. Although the absorption of heat is not sensible by means of temperature, it is trackable through solid-liquid mass fraction. The percent liquid multiplied by the latent heat of fusion and mass will equal the total energy absorbed

during the phase transition process at a given point in time. Thus, an incomplete phase transition of the complete form given in equation 2.3 can be expressed as:

$$\Delta Q = \int_{T_0}^{T_t} mc_p dT + m\chi_t \Delta H_t^\circ \tag{2.4}$$

when rising from temperature T_0 to transition temperature T_t where χ_t percent of the material has undergone phase transition from phase one (phase at T_0) to phase two (phase above T_t). In the context of the ice water example, equation 2.4 represents the transition from a solid block of ice at T_0 raising in temperature to $T_t = 0°C$ and melting χ_t percent to liquid. The corresponding incomplete transition from T_f in phase two to the same point, mid-transition, can also be expressed in a similar manner.

$$\Delta Q = \int_{T_f}^{T_t} mc_p dT - m(1 - \chi_t)\Delta H_t^\circ \tag{2.5}$$

Some other common applications that utilize phase change materials include commercial refrigeration units that utilize PCMs to create longer time constants to extend the time of heat rejection, thereby improving condenser efficiency [32]. PCMs have also been shown to improve heating time constants for organ transport containers, increasing the heating time constaint to maintain viability for up to 8 times longer than conventional insulation alone [33]. In particular, proposed applications as a heat storage mechanism for buildings is directly analogous to WaferSat. During the day, when it is typically warmer, buildings heat up, requiring air conditioning to maintain temperatures. At night, they cool down, potentially requiring heaters, representing an inefficient cycling of heat. PCMs have been proposed as insulating material to act as a thermal capacitor, storing heat during the day and releasing it at night, thereby reducing the need for active thermal control [34].

In these applications, the extension of the heating and cooling time constants allows for reduced active-control power expenditure to maintain a given temperature

range. These examples particularly highlight the benefits in the presence of temperature cycling, wherein the absorbed energy during a phase transition is then re-utilized in the cooling phase. The reduced power expenditure associated with heat storage in building structures can be extended to the more extreme eclipse-day cycling of a spacecraft in Earth orbit, enhancing survivability and operation.

2.1.3 Thermal Properties and Selection

In a mass-constrained system, a key goal for a phase change material is to maximize the ratio of thermal energy storage to mass. Thus, there are several key properties to consider when selecting phase change materials. These include:

- phase transition temperature, T_t
- specific latent heat capacity, H_t°
- specific sensible heat capacity, c_p
- thermal conductivity, κ_t
- matching of coefficients of thermal expansion (CTE)
- implementation and material compatibility

Phase transition temperature is a critical thermal parameter when selecting a phase change material. To maximize the utilization of latent heat storage, a transition point should be selected so that the oscillation of thermal energy utilizes the full latent heat capacity (not a partial transition). Additionally, the time of phase transition, t_t, is also governed by the rate of heat transfer. As shown in equation 2.6, the rate of radiative heat transfer from a black body, 1 to a grey body, 2 is proportional to the difference of the fourth power in body temperatures (the thermal gradient). Thus, for a given PCM, the heating/cooling time constant increase (the delay) is maximized

where the net rate of heat transfer is lowest (here, the lowest thermal gradient). The nature of the radiative thermal gradient also yields asymmetric heating and cooling rates of heat transfer. Therefore, careful selection of the PCM transition temperature may allow for maximization and tuning of the length of the phase transition and thus the increase to the effective time constant.

$$Q_{1-2} = \sigma \varepsilon_2 A_1 F_{1-2} (T_1^4 - T_2^4) \tag{2.6}$$

Though the main mode of heat storage in phase change materials is in the form of latent heat, the specific sensible heat capacity serves as a secondary heat storage mechanism as expressed in the first and third terms of equation 2.3 for a temperature range that spans above and below the transition temperature (corresponding to the desirable state of full phase transition). As this is not the primary mode of heat storage, it is also not a driving selection parameter, but nevertheless is an additional consideration to determine the full mass-specific heat storage capability of a PCM.

Thermal conductivity of the PCM will also determine effectiveness of latent heat storage. Efficient operation of heat storage is predicated upon the ability to transfer heat into and out of the material. PCMs with very low thermal conductivity will suffer from a reduced ability to utilize the full extent of the latent heat capacity (except in applications where the period of thermal oscillation is long enough to allow for equilibration with the PCM). When considering implementation of PCMs within a larger structure, consideration should be given to CTE mismatch and associated thermal stresses. Containment of multiple phases of the PCM must also be considered; e.g., containment for a solid-liquid PCM in liquid form.

Phase change materials can be classified into several main types, as shown in Figure 2-2: organic, inorganic, and eutectic [35]. The organic phase change material group further subdivides into two categories: paraffins and non-paraffins. The paraffins, or hydrocarbon chains of the alkane series, offer high-density latent heat of

fusion over a large temperature range of solid-liquid transition. Melting point and latent heat of fusion generally increase with length of the carbon chain. The main advantages of organic PCMs include low toxicity, inertness, low vapor pressure, and relatively low coefficient of thermal expansion. Some disadvantages include the need for containment in liquid form and relatively low thermal conductivity (this can be overcome, see section 2.1.4.

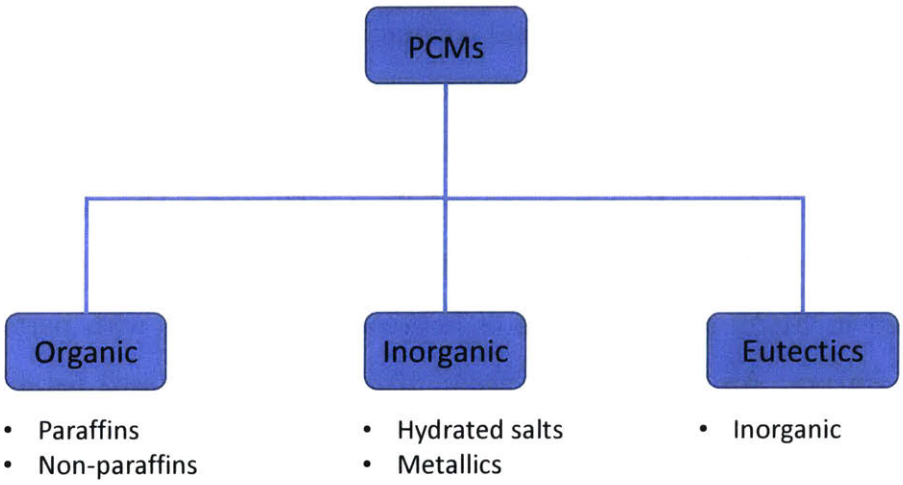

Figure 2-2: PCM Classification

There are two main types of inorganic PCMS: hydrated salts, and solid-solid metallics. Inorganic, hydrated salt PCMs are the most numerous. As solutions, hydrated salt PCMs suffer from non-uniform phase transition – the solvent may have a different melting point than the salt. Repeating cycling can cause separation and change the latent heat properties of the material. Solid-solid PCMs rely on a phase transition from a crystalline structure to amorphous. The solid-solid transition has the advantage of not requiring containment. Additionally, as metallics, they typically have high thermal conductivities. However the specific latent heat capacity is low

compared to paraffins. Eutectic compounds are solutions with a transition point below that of the constituents. Most are hydrated solutions and share similar properties to the inorganic hydrated salts. Eutectics are commonly used in applications where the desired transition temperature is low ($< 0°C$).

2.1.4 Implementation of Solid-Liquid Paraffins

Paraffin PCMs offer many favorable properties as latent heat storage mechanisms, however, they suffer from low thermal conductivity, slowing the heat transfer in and out of the material. Recent work on microencapsulation of paraffins in silicon nitride has shown a marked improvement in thermal conductivity whilst also containing the paraffin in liquid form. Known commercially as "Thermosorb", microencapsulation of paraffins can improve thermal conductivity by as much as 79% [7]. The paraffin is encased in Si_3N_4 at mass ratios of between 4% and 10% with particle sizes of 20 µm – 250 µm. An example of a 50 µm, 10% microencapsulated paraffin is shown in Figure 2-3.

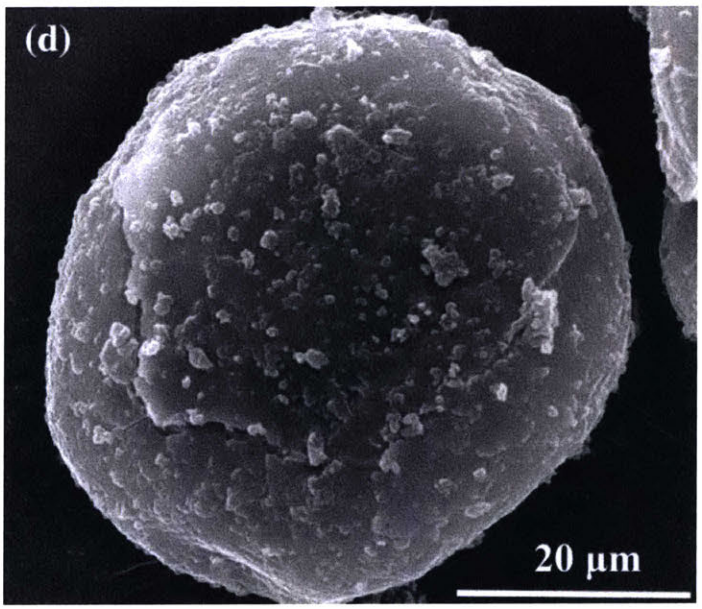

Figure 2-3: 10% Silicon Nitride Paraffin Microcapsule [7]

Chapter 3

Methodology

In order to evaluate the effectiveness of the implementation of phase change material as a thermal control architecture for WaferSat, an optimization process must be formalized. This chapter will describe the process in general form, then describe modeling specific to the WaferSat thermal problem at hand.

3.1 Problem Formulation

The optimization problem is defined as a minimization problem of a cost function that occurs in two stages according to fixed and continuous design parameter sets. The elements of the full design vector are classified into three categories: fixed parameters, z_D, discrete design parameters, x_D, and continuous design parameters, y_D. The bi-level optimization process is expressed in equation 3.1.

To evaluate the effectiveness of the thermal control architectures, the problem is expressed as a two-stage optimization problem with the objective of minimizing the cost function while satisfying the desired performance metrics and constraints. The cost function may consider several elements to evaluate the relative system impact

of the thermal control subsystem. Equation 3.1 below expresses the optimization formulation where the set z_D represents the fixed parameters, x_D represents the discrete design parameters, and y_D represents the continuous design parameters.

$$\begin{aligned} &\textit{minimize} && C_{discrete}(x_D, y_D, z_D) \\ &\text{subject to} && y_D \in \arg\min C_{continuous}(x_D, y_D, z_D) \\ & && g(x_D, y_D, z_D) \leqslant 0 \\ & && h(x_D, y_D, z_D) = 0 \\ & && x_D \in X_{discrete} \\ & && y_D \in Y_{continuous} \\ & && z_D \in Z \end{aligned} \tag{3.1}$$

Two forms of optimization are utilized, separating the decision variables into two types: continuous and discrete. Tables 3.2 and 3.3 show the classification of the variable types. Continuous variables are selected using a gradient-based optimization method and the discretized variables – denoted by an asterisk – are explored using a discrete search. The optimization process, shown in Figure 3-1 occurs in a series of steps described in the following subsections.

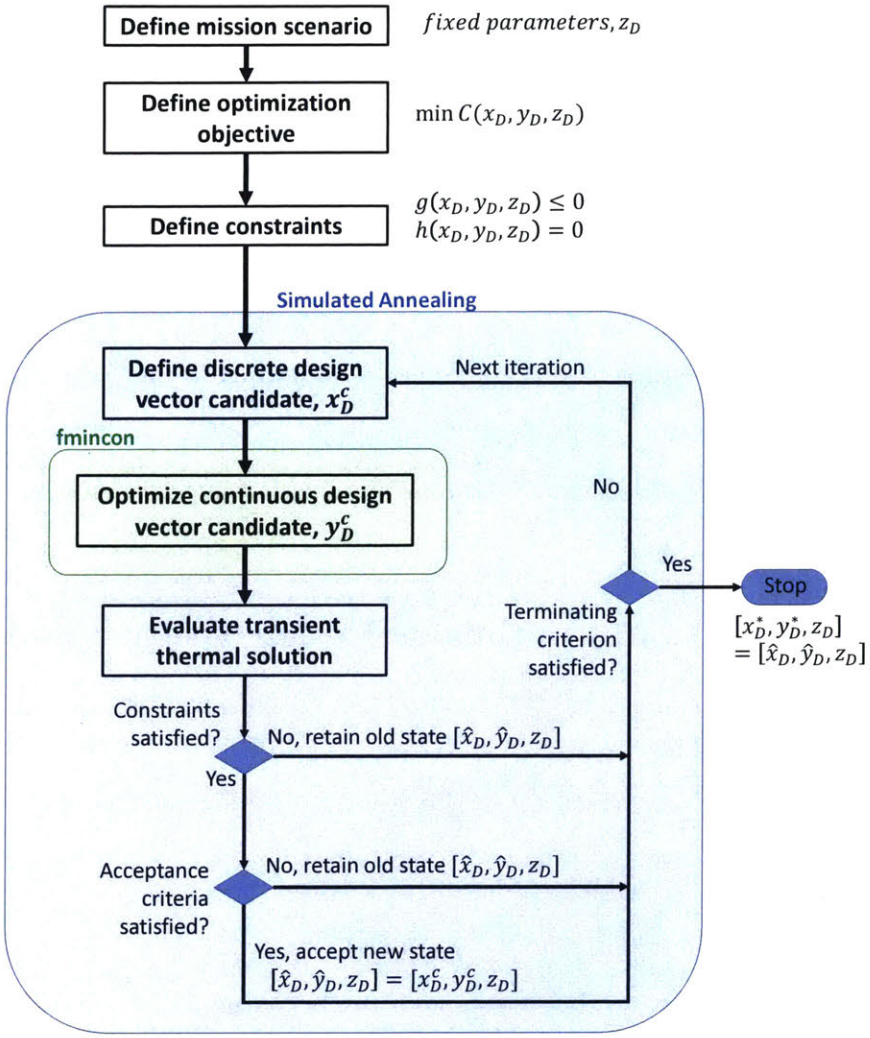

Figure 3-1: Optimization Process

3.1.1 Mission Scenario

First, a mission scenario for evaluation is defined. The mission scenario is largely defined by the payload and application, serving as an initialization of parameters that define the design space and constraints on the design parameters. The scenario defines the set of fixed parameters, z_D that do not vary within the current optimization, but may vary as other initializing scenarios are considered. This vector also includes constants.

3.1.2 Optimization Objective and Constraints

Next, the optimization objective is defined. This is expressed as a cost function to minimize throughout the optimization process. The cost is expressed as a function of the fixed parameters, z_D, the discrete variable design vector, x_D, and the continuous variable design vector, y_D.

Constraints are defined as quality constraints, expressed in function $h(x_D, y_D, z_D)$ and inequality constraints, expressed in function $g(x_D, y_D, z_D)$. The constraints model physical limits on variables, multi-variable limits, and performance requirements.

3.1.3 Discrete and Continuous Design Vector Candidates

Next, the discrete design vector is selected. The initial candidate vector of discrete design parameters, x_D^C is arbitrary; in the following iterations, the next discrete design vectors are selected using a probability distribution with the peak centered on the previous candidate vector.

Once the discrete candidate design vector is defined, the inner, gradient-based optimization minimizes over the continuous design vector, y_D^C. This inner-loop optimization solves over an abstraction of the transient problem with a steady state approximation. The full transient solution is evaluated in the next step.

3.1.4 Cost Evaluation and Next Iteration

The three vectors of parameters, z_D,x_D^C, and y_D^C are used to evaluate the transient temperature in quasi-steady state. If all constraints are satisfied, then the candidate composite design vector is a feasible solution. The first feasible solution is accepted as the state, $[\hat{x_D}, \hat{y_D}, z_D]$. An infeasible solution is never accepted and begins the next iteration. In successive iterations, feasible solutions are checked against an acceptance

criteria, shown in equation 3.2, where a is the acceptance probability, C_i is the cost of the current iteration design vector candidate, and T_i is the annealing temperature defined in equation 3.3. The annealing parameter, k_a a number between 0 and 1, defines the annealing rate.

$$a = \exp\left(\frac{C_i - \hat{C}}{T_i}\right) \tag{3.2}$$

$$T_i = (T_0)\, k_a^i \tag{3.3}$$

The acceptance criteria provides a probability of acceptance as the new state. An improved cost over the current state has an acceptance greater than 1, therefore is always accepted. Solutions with a higher cost than the state cost have a chance of accceptance that decreases as the annealing temperature decreases. Probabilistic selection of a higher cost state aids in prevention of convergence on local minima.

At the start of the next iteration, the next candidate, x_D^c is selected. The particular PCM and mass are each selected randomly over a normal distribution centered on the corresponding values of the current state (where the list of PCMs are ordered by melting temperature). Therefore, the next iteration is most likely a neighbor of the current state. The process terminates when the annealing temperature, T_i is less than a threshold value. At this terminating condition, the current state is identified as the optimal solution.

3.2 WaferSat Variable Sets

The fixed parameters in Table 3.1 represent physical constants that are not varied throughout the analysis. The fixed parameters refer to design variables that are

constant for a given evaluation case, but may be revised or changed to reflect a different scenario. Literature values of thermal properties are utilized for silicon-based solar arrays. Orbital parameters are defined within given prescribed mission scenarios. The prescribed scenarios do not encompass the full expected range of potential applications for WaferSat, rather they suggest several cases that may be motivated by several payload types and objectives. A range of continuous internal heat dissipative capacities will be explored, with the expectation that PCM inclusion may allow for system architectures with increased internal heat dissipative abilities. Similarly, the maximum and minimum allowable temperatures account for mission modes – such as operations and survival – and potentially differing temperature-constraining elements such as batteries or a payload itself.

Table 3.1: Fixed Parameters, z_D

Parameter	**Notation**
Solar irradiance	E_{sol}
Mean Earth Albedo	A_E
Earth IR flux	I_E
Wafer area	A_{waf}
Solar cell efficiency	η_{SA}
Solar cell emissivity	ε_{SA}
Solar cell absorptivity	α_{SA}
Orbit altitude	h
Upper temperature limit	T_{limH}
Lower temperature limit	T_{limC}
Internal heat dissipation	Q_{int}

The key design parameters are those that are altered within each evaluation to reach satisfaction of the constraints and produce a global minimum system cost.

Table 3.2: Discrete Design Parameters, x_D

Parameter	**Notation**
PCM melting point	T_m
PCM latent heat of fusion	H_f°
PCM specific heat capacity	C_p
PCM mass	m_{pcm}
Attitude vector	$\overline{\gamma}$

Table 3.3: Continuous Design Parameters, y_D

Parameter	**Notation**
Wafer top emissivity	ε_T
Wafer top absorptivity	α_T
Wafer bottom emissivity	ε_B
Wafer bottom absorptivity	α_B
Solar array physical fill factor	ϕ_{SA}

These parameter sets are listed in Tables 3.2 and 3.3, separated into two types. The continuously defined variables, y_D, include the key parameters that define thermal properties governing rates of radiative heat transfer such as the top and bottom emissivities and absorptivities, and solar array physical fill factor. Collectively, these properties define the effective thermal properties of both sides of the wafer. Due to their continuity and constitutive structure, these parameters are parsed using a gradient-based search. In contrast, the discrete design vector, x_D, is comprised of the set of phase change parameters from a subset of the alkane series of organic paraffins. The properties considered include melting point, latent heat of fusion, and specific heat capacity. These three properties are selected together, according to specific paraffins. Phase change mass is also discretized with step size selected to balance the resolution of the explored space with the extent of nodes in the full enumerated search space.

The objective of the optimization problem is to minimize the overall system impact of the PCM thermal control architecture while meeting several desired performance objectives. The system impact can expressed as a multi-element cost function consisting of PCM mass impact, occupied volume, occupied surface area (of thermal control or power elements that carry opportunity cost of surface usage: required solar array physical fill factor, controlled surface finish area), and constraints on wafer attitude. On WaferSat, the mass impact is at the center of these system impacts and dominates. As a simplification, in this thesis, the objective is to minimize required PCM mass. Required performance metrics include hot and cold temperature extremes, rate of power generation per orbit, and power available to the payload.

3.3 Subsystem Modeling and Interactions

There are several key subsystems and their associated interactions that are considered: orbits, attitude, power, and thermal. Together, the inter-related inputs and outputs govern the overall system impact cost and ability to meet performance requirements.

3.3.1 Subsystem Modules

The subsystem models are organized to share variables for inter-subsystem constraints, as shown in Figure 3-2. Parameters are shared; outputs of the subsystem models act as inputs to other modules to model the key elements of interdependency within the larger system. Transfer of outputs and inputs ensures that the multi-disciplinary constraints and objectives are jointly satisfied.

To prevent an infinitely recursive loop, the model must be initialized with several driving parameters. Unchangeable variables such as the constants and fixed parameters within an evaluation comprise this driving set. As described in section 3.1,

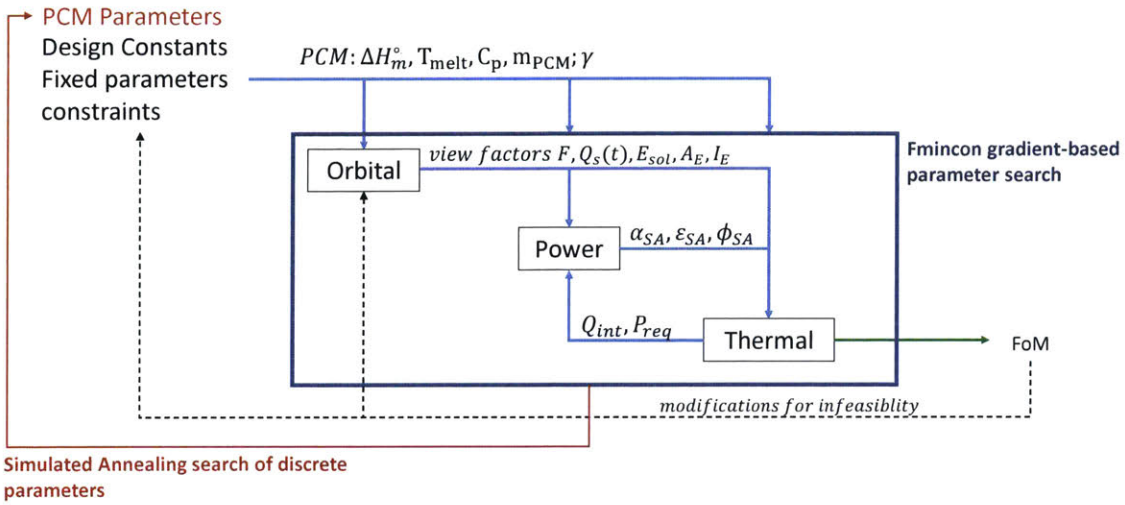

Figure 3-2: Subsystem Model Structure

the fixed parameters define the mission scenario to initialize the loop. The fixed parameters are only revised between evaluations to consider alternate cases; they may also be revised in the case that the continuous optimizer fails to converge – if there does not exist a feasible solution (in which case the fixed parameters and the constraining relations are relaxed to construct a feasible solution).

The three main subsystem models include orbits and attitude, thermal, and power. The orbital model tracks the attitude and position in the orbit in time, providing angles to the Sun, Earth, and free space for calculation of view factors in the thermal model. In the power block, the required power generation is influenced by integrated exposure time of the solar arrays on the top face. Power decisions are considered to be downstream of the discrete attitude decisions, therefore power parameters such as the physical fill factor are modified to meet the orbit average power generation requirement set by the average internal heat dissipation constraint. Selection of a solar array physical fill factor combined with the wafer top and bottom absorptivities and emissivities are utilized to calculate effective thermal radiative properties.

The inner loop of the three subsystem models is solved using the fmincon function

in MATLAB, a gradient-based optimizer to determine the sets of continuous variables. Constraints are modeled as equality or inequality conditions, setting bounds on variables as well as coupled parameter constraints. The discrete variables in the outer loop are solved using simulated annealing to search through a database of PCM material properties (in Appendix A).

3.3.2 Orbits and Attitude

The first subsystem to consider is the orbits and attitude subsystem. Outputs from this subsystem model govern the radiative view factors and thus the rates of thermal radiative energy transfer in and out of the system. Decisions in the orbits model are largely driven by the mission scenario, or Concept of Operations (CONOPS). Thus, the orbital parameters in this module are largely 'upstream' of the other modules, with its outputs primarily driving inputs to others.

For this thesis, some simplifying orbit assumptions are made. WaferSat is assumed to be in a circular orbit at an altitude of 400 km. WaferSat is also assumed to operate near zero β angle, the projected angle from the orbital plane to the Earth-Sun vector. Due to the anticipated relatively short operational lifetime, it is assumed that the duration of the mission will occur near the zero beta angle, so variation is not considered. The lack of variation establishes a quasi-static oscillation of heat, enabling consideration of the most effective usage of the PCM heat storage through phase cycling. Similarly, due to the anticipated short mission duration, seasonal variations of solar output are not considered – an average value is assumed.

A further simplification regarding eclipse is also made in which the eclipsed region behind the Earth is assumed to consist of a uniform cylindrical shape with radius matching that of the Earth (the umbra). In effect, the sun is represented by a flat wavefront. Thus, in its transit behind the Earth, WaferSat does not encounter the penumbra regions to either side of umbra, only a uniformly eclipsed region. The

number of distinct radiative differential equations is reduced to two: sunlight and uniform eclipse.

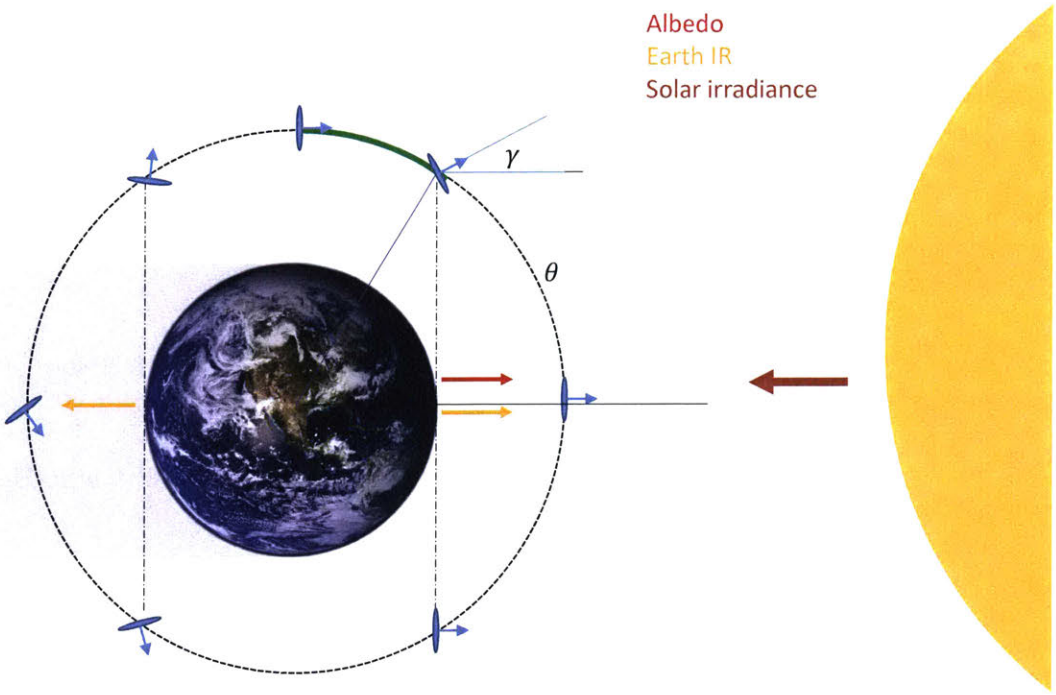

Figure 3-3: WaferSat Attitude, γ Angle

Throughout the orbit, the attitude of the spacecraft has a large impact on the radiative view factors. To reflect this impact, a single angle, γ is defined as the angle between the wafer top side (solar array side) surface normal and the Earth-Sun vector as shown in Figure 3-3. For simplicity, this angle is constrained to the orbital plane. Additionally, to enable search with the outer loop of the optimizer, the attitude is discretely defined over a set intervals in the orbit wherein γ is fixed for the duration of each interval. The vector of γ represents the attitude decisions at the start of each interval. For initial cases, γ is fixed in time to confine the number of searchable elements and evaluated permutations.

Consider the following set of potential motivating mission scenarios that define separate optimization cases and constraints:

Table 3.4: Heat source terms incident upon the wafer

#	Scenario	Description of γ Constraint
1	Always sun-facing	γ fixed to 0
2	Wafer bottom side nadir-facing	γ constrained to maintain constant view factor to Earth
3	Thermally-favorable attitude	γ constraint relaxed, varies to minimize PCM mass
4	Defined time of selective attitude pointing	γ constrained to provide specified time of selective pointing per orbit
5	Predefined attitude profile	γ constrained to follow fully defined attitude profile over orbit

In all scenarios, the objective is to minimize the required PCM mass to meet the system constraints and thermal temperature requirements. In case number 1, the attitude of the wafer is fixed such that the normal of the top surface (the solar array side) is aligned with the Earth-Sun vector for all time (γ angle of zero) as shown in Figure 3-4. Therefore, in the sunlit portion of the orbit, the view factor of the top surface to the Sun remains constant. The top and bottom wafer face view factors to the Earth vary in time.

The Sun-facing reference orbit case represents a mission scenario where maximization of solar exposure. For a given constant power requirement, the result is a reduced required solar cell area (ϕ_{SA}), freeing up surface area for other devices. The sun-facing scenario also represents the worst-case hot thermal conditions and can serve as a bounding case for the required PCM mass.

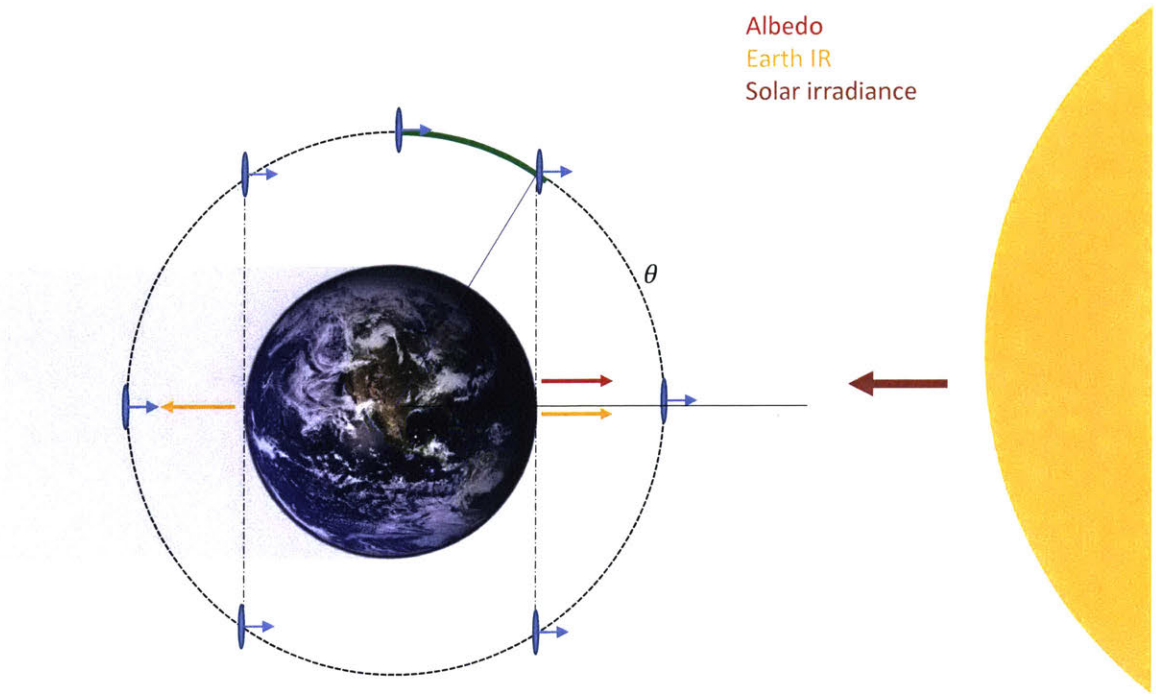

Figure 3-4: Sun-Facing Reference Attitude Profile, $\gamma = 0$ for all time

In case number 2, the normal of the bottom surface is always aligned with the wafer-Earth vector, depicted in Figure 3-5. In this 'tidally locked' profile, the wafer bottom surface to the Earth is fixed at maximum while the view factors to the sun vary with time and position.

The nadir-facing orbit is an orbital profile where pointing towards the Earth is maximized, representing a scenario with prioritization of pointing for an Earth-facing payload or downlink.

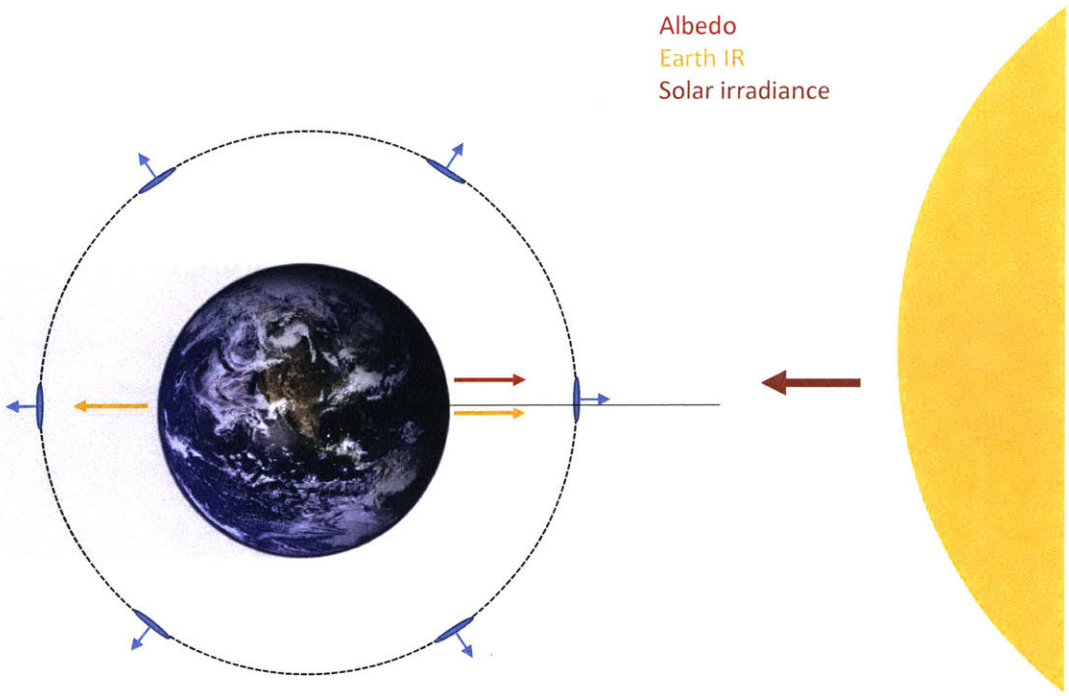

Figure 3-5: Nadir-Facing Reference Attitude Profile

Cases 3 through 5 involve variable profiles in which the attitude is not fixed relative to either the Earth or Sun. In these cases, the profile is discretized into evenly-spaced decision periods throughout the orbit. At the start of each phase, the angle γ is defined and remains constant for the duration of that phase. In case 3, a series of attitude decisions that provide favorable thermal view factors is constructed to minimize the phase change material mass. Note that the vector of attitude decisions is still subject to the constraint to provide sufficient power generating capability over the course of an orbit (described in section 3.3.5). The phase change mass in this condition is minimized to be sufficient to meet thermal conditions in this attitude profile. With this phase change mass, the attitude profile must be strictly maintained to continue to meet the thermal conditions. Given the constraints on attitude, the scenario might be suitable for payload and downlink applications where pointing is

not a concern.

If the minimum PCM mass condition depends on the thermally favorable attitudes in case 3, that attitude profile must be followed to meet the system constraints. The final two cases present the ability to deviate from the thermally-favorable profile through additional margin created by extra phase change material. Attitude 'freedom' refers to the ability to change the attitude to an arbitrary or desired orientation at a decision point. As the relative positions of the vectors from the wafer to the Sun, Earth, and free space vary throughout the orbit, so too does the sensitivity of required extra phase change material mass to attitude variation. At some positions in the orbit the marginal gain in attitude freedom is higher per extra gram of phase change mass.

In case 4, a constraint on the minimum desired time-per-orbit of attitude freedom is applied. As the position of the attitude variation is not constrained, the orbital positions where the increase in phase change material mass is least sensitive are selected. In this way the desired free pointing time per orbit is satisfied, but is constrained to locations, not specified by the payload. Therefore, case 5 adds further constraints to case 4 by specifying locations in the orbit where the attitude is defined. This scenario might represent a case where a desired imaging target on the Earth is required and the attitude must be specified at the overpass.

3.3.3 Thermal

To evaluate the impact of phase change material, the transient thermal problem must be solved. The temperature of the spacecraft, T_{waf} is expressed in equation 3.4 as a function of the net heat source term, Q_S, top wafer surface thermal radiation, Q_{radT}, and bottom surface thermal radiation, Q_{radB}.

$$\frac{d}{dt}(mCpT_{waf}) = Q_S - Q_{radT} - Q_{radB} \tag{3.4}$$

The net heat, Q_S is expressed in equation 3.5 as the sum of 10 heat source terms.

$$Q_S = Q_{int} + Q_{S-SA} + Q_{S-T} + Q_{S-B} + Q_{A-SA} + Q_{A-T} + Q_{A-B} + Q_{I-SA} + Q_{I-T} + Q_{I-B} \quad (3.5)$$

The varying rates of thermal heat transfer in and out of WaferSat are heavily influenced by view factors, or the fraction of radiated thermal energy from one surface that is incident upon another.

The Wafer has 3 unique surfaces that are considered to be uniform in terms of thermal properties: Wafer solar array area (partial surface area occupied on the top surface only), exposed wafer top surface (this 'exposed' area need not be bare silicon, it is assumed that it may be absorptivity/emissivity controlled with coatings), and the wafer bottom surface (independently absorptivit/emissivity-controlled from the top surface). There are 3 heat source elements considered: solar irradiance, Earth albedo, and Earth IR. There are 9 heat source elements that are incorporated as part of the thermal transient equation as shown in Table 3.5.

Table 3.5: Heat sources terms incident upon the wafer

Heat source	**Incident Surface**	**Term**
Solar Irradiance	Solar Array area	Q_{S-SA}
	Wafer top area	Q_{S-T}
	Wafer bottom area	Q_{S-B}
Earth Albedo	Solar Array area	Q_{A-SA}
	Wafer top area	Q_{A-T}
	Wafer bottom area	Q_{A-B}
Earth IR	Solar Array area	Q_{I-SA}
	Wafer top area	Q_{I-T}
	Wafer bottom area	Q_{I-B}

The rates of heat flow into WaferSat are summarized in the following equations with consideration of solar irradiance, albedo, and Earth IR incident upon all wafer surfaces. They can be summarized generally according to equation 3.6 where each source term is the product of the source flux density, E_{flux}, effective area of incidence of the particular surface, A_{eff}, and a wavelength-dependent absorptance parameter, Λ. The specific source terms are summarized in more detail in Table 3.6.

$$Q_{source} = E_{flux} A_{inc} \Lambda \tag{3.6}$$

Table 3.6: Incident Heat Source Terms

Source term	**Source flux density**	**Area of Incidence**	**Absorptive modifier**
Q_{source}	E_{flux}	A_{inc}	Λ
Q_{S-SA}	E_{sol}	$A_{waf} f_{S-T} \phi_{SA}$	α_{SA}
Q_{S-T}	E_{sol}	$A_{waf} f_{S-T} (1 - \phi_{SA})$	α_{SA}
Q_{S-B}	E_{sol}	$A_{waf} f_{S-B}$	α_B
Q_{A-SA}	$A_E E_{sol}$	$A_{waf} f_{E-T} \phi_{SA}$	α_{SA}
Q_{A-T}	$A_E E_{sol}$	$A_{waf} f_{E-T} (1 - \phi_{SA})$	α_T
Q_{A-B}	$A_E E_{sol}$	$A_{waf} f_{E-B}$	α_B
Q_{I-SA}	I_E	$A_{waf} f_{E-T} \phi_{SA}$	ε_{SA}
Q_{I-T}	I_E	$A_{waf} f_{E-T} (1 - \phi_{SA})$	ε_T
Q_{I-B}	I_E	$A_{waf} f_{E-B}$	ε_B

Note that by Kirchoff's law of thermal radiation, the emissive and absorptive terms are functions of wavelength and are equal for a common wavelength (or band of wavelengths):

$$\Lambda \equiv \alpha_\lambda = \varepsilon_\lambda \tag{3.7}$$

As a convention, α denotes absorptivity and emissivity for visible light wavelengths, while ε denotes absorptivity and emissivity for infrared wavelengths.

The heat sources are based on source flux densities, so the term governing variation of the heat source terms in time is given by the changes in the projected receiving area on the wafer. There are 4 generalized projection terms: Wafer top surface to sun, wafer top surface to Earth, wafer bottom surface to sun, and wafer bottom surface to Earth. These are shown in equations 3.8 through 3.11. In the Sun to wafer cases, the modifying term is governed by γ and in the Earth to wafer cases, the modifying term is governed by the effective angle to Earth which includes both the true anomaly, θ and γ. True anomaly, θ, is shown in Figure 3-3 and is defined as the angle subtended by WaferSat about the Earth, referenced to the Earth-Sun vector. These terms manifest in the heat source terms incident upon the wafer surfaces as heat flux elements as shown in Table 3.6. The terms are described as piecewise functions to maintain generality for arbitrary angles of θ and γ. Thus, they are set to zero when a receptive side of the wafer is not in view of a heat source.

$$f_{S-T} = \begin{cases} 0 & \cos(\gamma) < 0 \\ cos\,(\gamma) & \cos(\gamma) \geqslant 0 \end{cases} \tag{3.8}$$

$$f_{S-B} = \begin{cases} 0 & \cos(\gamma - \pi) < 0 \\ \cos(\gamma - \pi) & \cos(\gamma - \pi) \geqslant 0 \end{cases} \tag{3.9}$$

$$f_{E-T} = \begin{cases} 0 & \cos\,(\theta - \gamma) < 0 \\ \cos\,(\theta - \gamma) & \cos\,(\theta - \gamma) \geqslant 0 \end{cases} \tag{3.10}$$

$$f_{E-B} = \begin{cases} 0 & \cos(\theta - \gamma - \pi) < 0 \\ \cos(\theta - \gamma - \pi) & \cos(\theta - \gamma - \pi) \geqslant 0 \end{cases} \tag{3.11}$$

The thermal radiative terms to free space for the top and bottom wafer surfaces are expressed in equations 3.12 and 3.13. The rates of radiation are functions of the wafer area, A_{waf}, emissivity, ε, wafer temperature, T_{waf} and view factors, F_*.

$$Q_{radT} = \left(1 - F_{T-E} - F_{T-S}\right) A_{waf} \varepsilon_T \sigma \left(T_{waf}^4 - T_{space}^4\right) \tag{3.12}$$

$$Q_{radB} = \left(1 - F_{B-E} - F_{B-S}\right) A_{waf} \varepsilon_B \sigma \left(T_{waf}^4 - T_{space}^4\right) \tag{3.13}$$

To define radiative view factors from each wafer side to either the Sun or Earth, fractions of the full radiative view factor are calculated. Each wafer surface is assumed to have a full hemispherical radiative view factor of 2π steradians. The Sun, at a long distance of 1 astronomical unit (AU) is approximated to occupy the projected area on the celestial hemisphere at a distance of 1 AU. These simplified view factors are expressed in equations 3.14 and 3.15.

$$F_{T-S} = \begin{cases} 0, & \cos(\gamma) < 0 \\ cos(\gamma)\left(1 - \cos\left(\arctan\left(\frac{R_{sun}}{AU}\right)\right)\right), & \cos(\gamma) \geqslant 0 \end{cases} \tag{3.14}$$

$$F_{B-S} = \begin{cases} 0, & \cos(\gamma + \pi) < 0 \\ \cos(\gamma + \pi)\left(1 - \cos\left(\arctan\left(\frac{R_{sun}}{AU}\right)\right)\right), & \cos(\gamma + \pi) \geqslant 0 \end{cases} \tag{3.15}$$

The radiative view factors to the Earth are calculated according to the near field. Instead of a flat projection on the hemispherical view factor, the Earth radius defines an occupied cone angle, $2\theta_0$ as shown in Figure 3-6. When the hemispherical full view factor of a side encompasses the full cone, the view factor is at a maximum, defined as the ratio of the solid angle of the cone to 2π steradians. When the angle of the surface normal relative to the wafer-Earth vector is greater than the cone half angle, θ_0, the edge of the side view factor is transiting the surface of the Earth, therefore there is a cosine term reduction as shown in equations 3.16 and 3.17. The view factors appear in the radiator calculations for the top and bottom wafer surfaces. Like the wafer-Sun view factors and heat source modifiers, these view factors are defined with non-specificity so that any attitudes and orbital positions will set corresponding view factors to zero in the case of zero view.

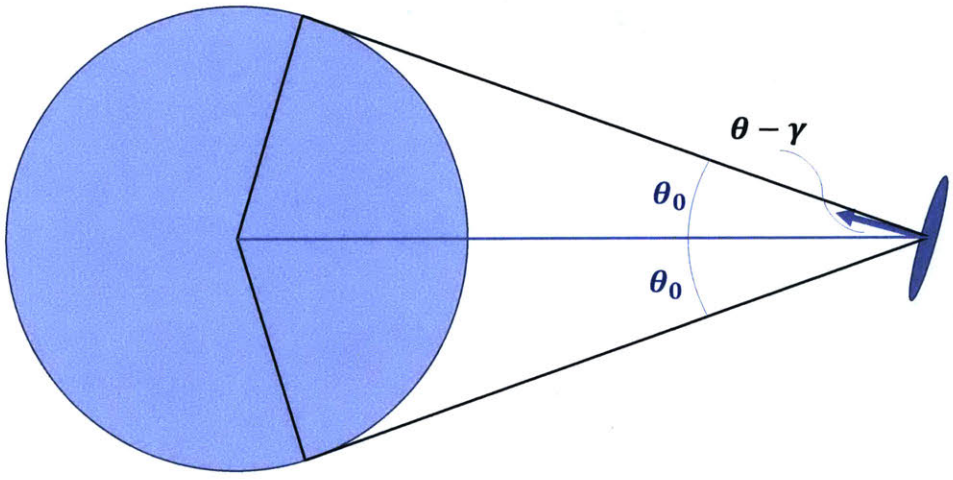

Figure 3-6: Earth view factor

$$F_{B-E} = \begin{cases} 0, & |\theta - \gamma| > 2\arcsin\left(\frac{R_E}{R_E+h}\right) \\ 1 - \cos\left(\arcsin\left(\frac{R_E}{R_E+h}\right)\right), & \arcsin\left(\frac{R_E}{R_E+h}\right) \leqslant |\theta - \gamma| \leqslant 2\arcsin\left(\frac{R_E}{R_E+h}\right) \\ \cos\left(\frac{\pi(\theta-\gamma)}{2\arcsin\left(\frac{R_E}{R_E+h}\right)}\right)\left(1 - \cos\left(\arcsin\left(\frac{R_E}{R_E+h}\right)\right)\right), & |\theta - \gamma| \leqslant \arcsin\left(\frac{R_E}{R_E+h}\right) \end{cases} \tag{3.16}$$

$$F_{T-E} = \begin{cases} 0, & |\theta - \gamma - \pi| > 2\arcsin\left(\frac{R_E}{R_E+h}\right) \\ 1 - \cos\left(\arcsin\left(\frac{R_E}{R_E+h}\right)\right), & \arcsin\left(\frac{R_E}{R_E+h}\right) \leqslant |\theta - \gamma - \pi| \leqslant 2\arcsin\left(\frac{R_E}{R_E+h}\right) \\ \cos\left(\frac{\pi(\theta-\gamma-\pi)}{2\arcsin\left(\frac{R_E}{R_E+h}\right)}\right)\left(1 - \cos\left(\arcsin\left(\frac{R_E}{R_E+h}\right)\right)\right), & |\theta - \gamma - \pi| \leqslant \arcsin\left(\frac{R_E}{R_E+h}\right) \end{cases} \tag{3.17}$$

3.3.4 Phase Change Material

Phase change materials offer an increase in overall heat storage capacity when passing through the phase transition point. Therefore PCM mass does not impact the temperature equilibration points, rather, it affects the effective rate of equilibration. In quasi-static heat cycling – as in an the day-night cycling of an orbit – the increase in effective time constant can prevent equilibration. If the time to equilibrate is extended beyond the period of the heating or cooling stages, the temperature cycling band (defined by the full range bounded by maximum and minimum temperatures) is truncated, limiting the temperature extremes attained.

To model the effective time constant change due to the introduction of latent heat storage at constant temperature, the transient oscillation must be propagated forward in time. Two separate differential equations for the temperature transient are solved: the cooling case, representing the eclipse portion of the orbit, and the

heating case, representing the sunlit portion of the orbit. Both of these are expressed as forms of equation 3.4 with differing heat source terms based on solar exposure. In the cooling case, the solar flux density term, E_{sol} is set to 0. Oscillation is initialized from a starting temperature T_0 at the beginning of the eclipse portion of the orbit. The cooling differential equation is first solved for the duration of eclipse without accounting for latent heat storage. In the event of a melting temperature crossing – a phase change – the time taken to transition is calculated.

To account for partial phase transitions in which only a fraction of the full phase change material mass undergoes a phase transition before the end of an eclipse or sunlit period, the percentages of solid and liquid mass are tracked in time. In this over-saturated case, only the percentage of previously transitioned material is available. The calculation of the duration of the temperature pause during phase transition for freezing and melting are shown in equations 3.18 and 3.19 respectively.

$$t_f = \frac{m_{PCM} H_m^\circ L_{frac}}{Q_{net}^f(T_m)} \tag{3.18}$$

$$t_m = \frac{m_{PCM} H_m^\circ (1 - L_{frac})}{Q_{net}^m(T_m)} \tag{3.19}$$

In both equations, L_{frac} represents the liquid fraction (and $(1 - L_{frac})$ correspondingly represents the solid fraction), H_m° is the specific latent heat of fusion, and $Q_{net}^f(T_m)$ and $Q_{net}^m(T_m)$ are the net heat flow rates at the melting temperature, T_m, for freezing and melting respectively.

More specifically, if the net heat flow gradient is considered to vary in time with changing view factors due to orbital motion or attitude changes, the length of the temperature pause is expressed as the difference in the limits of an integral of the

time-dependent net heat gradient over the transition. The freezing case:

$$m_{PCM} H_m^\circ L_{frac} = \int_{t_{p0}}^{t_{p1}} Q_{net}^f(t, T_m) dt \tag{3.20}$$

The melting case:

$$m_{PCM} H_m^\circ (1 - L_{frac}) = \int_{t_{p0}}^{t_{p1}} Q_{net}^m(t, T_m) dt \tag{3.21}$$

where the length of temperature pause in both cases is expressed as:

$$t_{Tpause} = t_{p1} - t_{p0} \tag{3.22}$$

In the event of a full phase transition where the time at t_{Tpause} is still within the current cooling or heating period, the solution to equation 3.4 continues to propagate forward. At the end of either the eclipse or sunlit portion of the orbit, the current temperature is used as the starting temperature for the heating or cooling form of equation 3.4 for the next orbital stage. The process is repeated for several full orbital periods to establish a stable quasi-static oscillation. Any temperature extremes attained prior to the convergence on quasi-static oscillation are not considered as these are dependent on the assumed initialization temperature and starting point in the orbit. In the analysis cases in this thesis, temperatures are initialized at 25° C at the start of eclipse with fully solid PCM mass.

3.3.5 Power

WaferSat is envisioned to eventually become a small satellite platform, capable of supporting small payloads. For the purposes of this thesis, power available to a potential payload is assumed to be directly proportional to capability of a potentially hosted payload. The power subsystem models the orbit average rate of power generation.

The power subsystem must satisfy a constraint expressed in equation 3.23, which states that the mean energy generation by the solar arrays per orbit is less than or equal to the orbit average internal energy dissipation.

$$\int_{t_{s0}}^{t_{sf}} A_{waf}\phi_{SA}f_{S-T}E_{sol}\eta_{SA}dt \geqslant Q_{int}P_{orbit} \tag{3.23}$$

The left side of equation 3.23 is the total power generated per orbit, defined as an integral of solar array power generated from the start of sunlight at t_{s0} to the end of sunlight, t_{sf}. The effective solar array collection area is the product of the wafer area, A_{waf}, the solar array physical fill factor, ϕ_{SA}, and the projection term from the sun to wafer top, f_{S-T}. η_{SA} is the solar array efficiency, and E_{sol} is the solar flux density. On the right hand side, Q_{int} is the continuous heat dissipation term and P_{orbit} is the orbital period. The product of these two terms is the orbit average energy demanded by the system.

The internal heat dissipation term is defined as the sum of payload power, $Q_{payload}$ and heater power, Q_{heater} as shown in equation 3.24. A decision parameter, λ is shown in equation set 3.25 to express Q_{int} as the upper bound on $Q_{payload}$. When $\lambda = 1$, all internal heat dissipation is due to payload operation. For values of λ less than 1, the internal heat dissipation is shared between the payload and internal heaters. The system is required to dissipate Q_{int}, which generates the primary constraint for power demand.

$$Q_{int} = Q_{payload} + Q_{heaters} \tag{3.24}$$

$$\begin{aligned} Q_{payload} &= \lambda Q_{int} \\ Q_{heaters} &= (1-\lambda)\, Q_{int} \\ \lambda &\in [0,1] \end{aligned} \tag{3.25}$$

There are several key parameters defining the rate of power generation that include solar cell efficiency, solar array physical fill factor (the area percentage coverage on the wafer top side), and time vector of solar angle of incidence on the solar array. For a given time-series vector of solar angles of incidence as defined by angle γ and solar cell efficiency (of a single-crystal silicon solar cell), the solar array physical fill factor, ϕ_{SA} must change to ensure that the orbit average power generation requirement is met.

3.4 Summary

The methodology to evaluate PCM thermal control architectures is presented in this chapter. The problem is posed as a minimization of the required PCM mass to meet thermal requirements over a design space composed of discrete and continuous design parameter sets. Modeling of orbits and attitude, thermal, and power contribute to constraints on the design space. A simplified example is presented in Chapter 4 to illustrate the operation of the PCM. Finally, the full methodology is utilized in two scenarios in Chapter 5.

The MATLAB code to implement the methodology is located in the following GitHub repository: https://github.mit.edu/SSL/WaferSat

Chapter 4

PCM Operational Modes

To help illustrate the effect of introduction of PCM mass, a simplified example is given. In this example, several potential operating modes for the PCM are presented to show the sensitivity of temperature oscillation range to the selected melting point. As detailed in section 2.1, efficient operating conditions for PCMs rely on energy flow balance about the melting point, completely passing through the melting temperature, indicating 100% transition from solid to liquid and vice versa. There are six distinct operating modes organized into several categories in Table 4.1.

Table 4.1: PCM Modes of Operation

Mode	**PCM description at quasi-steady state**
1	Full solid-liquid phase transition
2	Partial solid phase transition, full liquid phase transition
3	Partial liquid phase transition, full solid phase transition
4	No phase transition, liquid phase only
5	No phase transition, solid phase only
6	Partial liquid phase transition, full solid phase transition

To define the temperature bias we first define the center of energy oscillation. For

a given stable heating and cooling cycle, there will exist a temperature, T_{center}, at which the magnitude of the time integral of heat flows above T_{center} in one heating cycle is equal to that below T_{center} in one cooling cycle. In other words, the magnitude of the heat transfer into the wafer to raise the temperature from T_{center} to the peak temperature, T_{max} is equal and opposite to the magnitude of the heat transfer to lower the temperature from T_{center} to the minimum temperature, T_{min}. Note that due to varied specific heat capacity with temperature, T_{center} is distinct from the midpoint of temperature extremes.

We define the relative temperature bias as the relation of T_{center} relative to the melting point of the PCM, T_{mp}. Hot bias refers to the condition where $T_{center} > T_{mp}$, and cold bias refers to the condition where $T_{center} < T_{mp}$. Both cases result in asymmetric effects on the hot and cold temperature extremes as more PCM mass is added. When $T_{center} = T_{mp}$ it is said to be neutral, or there is no energy bias. Melting and freezing of the PCM is balanced, yielding a special case of constant temperature for all time when sufficient PCM mass is reached (for steady thermal energy oscillation).

Within each of the bias cases, there are sub-regimes of PCM mass denoting level of completeness of the phase transition. As described in section 2.1.1, there are two distinct modes of heat storage in phase change materials: sensible and latent heat storage. The three defined sub-regimes are defined by the completeness of the phase transition during each orbit, denoting the split of energy storage between the latent and sensible modes. Mode 1, which represents a full phase transition in the heating and cooling cases is common to all bias regimes. Modes 2 and 3 are mirrored partial transition cases for hot and cold bias respectively. Modes 4 and 5 both represent no phase transition, in liquid only and solid only states respectively. Mode 6 represents a partial phase transition in both solid and liquid phases in a neutral regime.

The distinct operating modes and regimes are shown in the following examples. To construct these cases, some simplifications are made. To demonstrate the regimes

of PCM operation, a single phase change material, pentadecane, is considered. The properties of pentadecane are summarized in table 4.2. Additionally, to simplify the heat equations, the two orbital states of eclipse and sunlit portions are switched in binary fashion from a position at opposition with the sun from Earth (for the eclipse duration) and a position at conjunction with the sun from Earth for the sunlit portion of the orbit. These two positions are shown in Figure 4-1. The true anomaly, θ, and attitude angles, γ, are held constant for the duration of each orbital phase, eliminating the variation in view factors, F_* and incident heat terms, f_*. Therefore, in the transient solution to equation 3.4, the heat source term, Q_S, the wafer top radiated heat, Q_{radT}, and the wafer bottom radiated heat, Q_{radB} each take a constant value in eclipse and another constant value in sunlight.

$$\frac{d}{dt}(mCpT_{waf}) = Q_S - Q_{radT} - Q_{radB} \qquad \text{(3.4 revisited)}$$

Table 4.2: Properties of Pentadecane

Property	**Value**
Melting point	10° C
Latent heat of fusion	$161\,\mathrm{J\,g^{-1}}$
Specific heat capacity	$2.21\,\mathrm{J\,g^{-1}\,K^{-1}}$
Density	$0.77\,\mathrm{g\,cm^{-3}}$
Chemical formula	$CH_3\,(CH_2)_{13}\,CH_3$

To artificially create the hot and cold bias heat cases, the internal heats are altered to artificially high or low values so as to create a net heat flow to adjust the center of oscillation relative to the melting point of pentadecane.

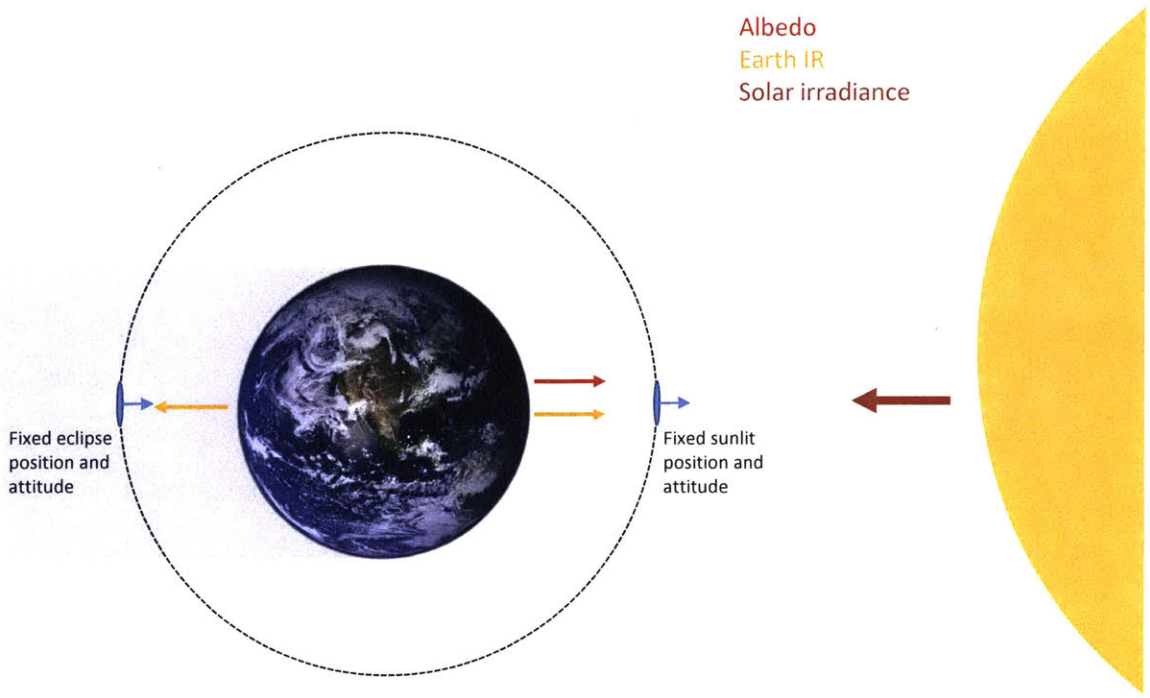

Figure 4-1: Binary Orbit Assumption

The design vectors are constrained as shown in Tables 4.3 and 4.4. All design parameters take constant values with the exception of PCM mass, m_{PCM}, and internal heat, Q_{int}. The selection of the internal heat value will determine the bias relative to the melting point of pentadecane. The PCM mass values represent a low, medium, and high quantities of PCM in each bias regime to illustrate the modes of operation.

Table 4.3: Simplified Discrete Design Parameters, x_D

Parameter	Notation	Value
PCM melting point	T_m	10° C
PCM latent heat of fusion	H_f°	161 J g^{-1}
PCM specific heat capacity	C_p	2.21 J g^{-1} K^{-1}
PCM mass	m_{pcm}	Variable: [5; 30; 80] g
Attitude vector	$\overline{\gamma}$	0
Internal Heat	Q_{int}	Variable: [10; 3; 8.3] W

Table 4.4: Simplified Continuous Design Parameters, y_D

Parameter	Notation	Constant Value
Wafer top emissivity	ε_T	0.3
Wafer top absorptivity	α_T	0.4
Wafer bottom emissivity	ε_B	0.3
Wafer bottom absorptivity	α_B	0.4

4.1 Hot Bias Relative to Transition Temperature

The hot bias case is defined where the temperature center of energy oscillation is higher than the phase transition temperature. A hot bias case is demonstrated in Figure 4-2 where the internal heat term is arbitrarily high to induce phase transition of the pentadecane near the lower end of temperature oscillation. The spacecraft temperature oscillation in time at quasi-steady state is shown for a 'low', 'medium', and 'high' phase change mass case (representing modes 1, 3, and 5 respectively). The shaded regions represent the eclipse portion of the orbit.

The low phase change mass case is shown in green and labeled mode 1 in Figure 4-3. In this case, which represents the hot-biased, full solid-liquid phase transition, the temperature decreases to the freezing point at 10° C where the temperature remains constant while the phase change mass melts; the time for this process is given by

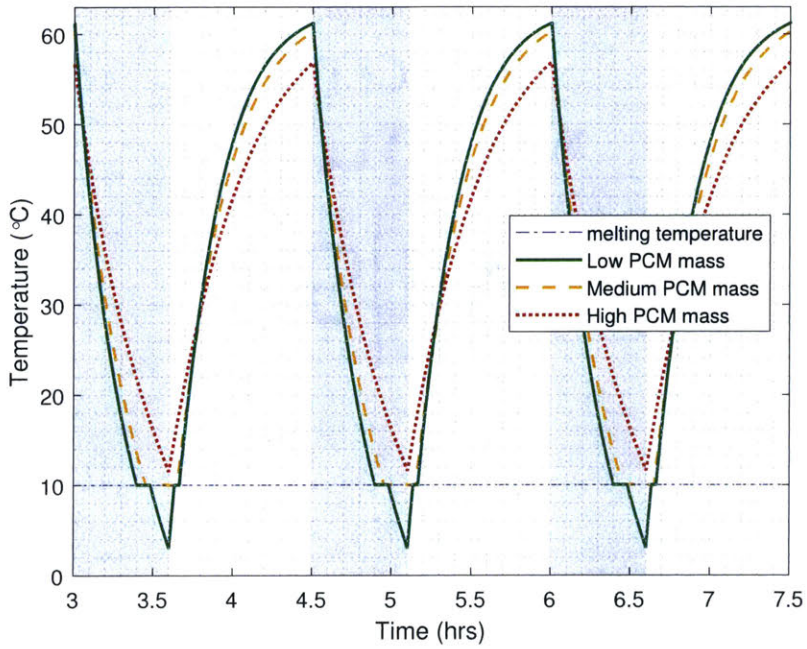

Figure 4-2: Hot-Biased Quasi-Steady State Temperature Oscillation for 3 PCM masses

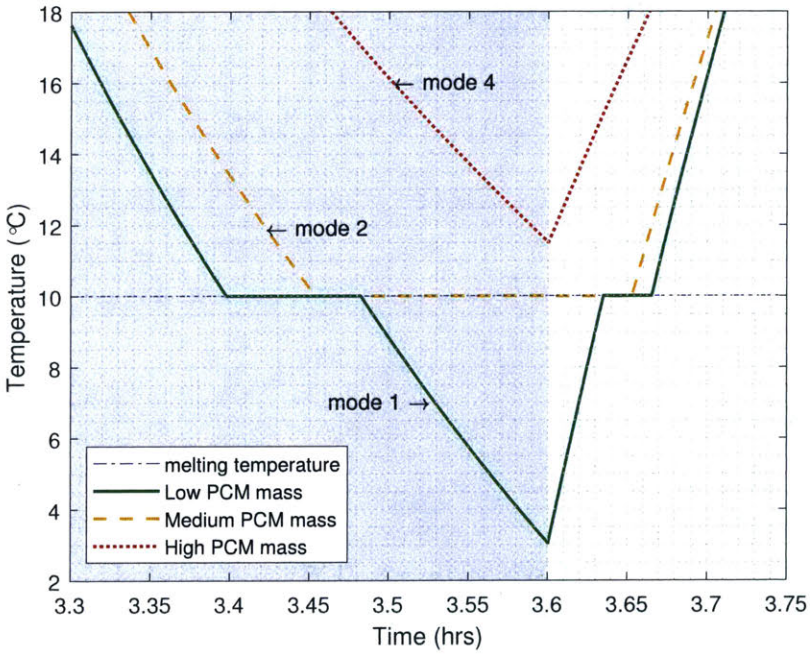

Figure 4-3: Zoom in of figure 4-2 PCM Operation

equation 3.18. At this mass, the phase change material completely freezes before the end of the eclipse portion and the temperature is allowed to continue to decrease. At the start of the sunlit portion of the orbit, the temperature rises until it reaches the melting point once again. The thermal gradient during heating is much higher than that during eclipse. Therefore, the duration of melting is much shorter due to a higher net heat flow rate in equation 3.19. Further increases in phase change mass increase the energy storage capacity at constant temperature, thus lengthening the temperature pause and effectively clipping the lower temperature peak.

The medium phase change mass case, representing the hot-biased, partial solid phase transition, full liquid phase transition is shown in dashed yellow and labeled mode 2. In this mode, there is sufficient mass to cause a saturation of PCM mass – the addition of more phase change mass does not cause an increase in the time of the temperature pause, since the end of the eclipse is reached before the entirety of the mass is frozen. Likewise, during heating, the percentage solid that is available to absorb latent heat is limited. The fraction of phase change mass that never fully freezes goes un-utilized as phase change material. It does have a small contribution to sensible heat storage through the addition of mass that manifests as a contribution only to term 1 of equation 2.4. It is also useful to note the asymmetry in the effect on the hot and cold extremes. In the increase of phase change mass from the low to medium mass, the minimum temperature rises from 3° C to the melting point at 10° C. However, the hot temperature extreme is only marginally decreased. The relative bias in this case causes a more pronounced effect on the cold extreme than the hot and it can be said that there is a higher contribution to the cooling time constant than to that of heating. The asymmetry of impact can be useful in conditions where only one temperature constraint is tight, or near its limit, while the other is slack.

All matter has energy storing capacity as temperature increases. Therefore, as a secondary effect (in magnitude) of the addition of latent heat storage mass, there is a corresponding increase in total sensible heat capacity which has an influence

on the effective heating and cooling time constant. This increase in sensible heat capacity can be observed in the shallowing of the cooling and heating temperature curves from the low to medium mass case. The effect is slight, but large quantities of mass can provide higher increases to sensible heat capacity as shown in the dotted red, high mass case, labeled mode 4. In this mode, the amount of phase change mass is increased significantly beyond the saturation point of case 2 such that the cooling curve shallows enough to the point where the temperature at the end of eclipse is above the melting point. Therefore, no phase transition ever occurs, and the only contribution of the PCM is as a sensible heat storage mechanism.

A comparison of the relative impact on temperature range is shown in Figure 4-4 in which the hot and cold temperature extremes are plotted against phase change material mass. The three distinct operating modes can clearly be observed in the cold temperature extreme plot. In mode 1, shown in green from 0 to 10 grams, we see the highest mass-specific increase in the cold temperature extreme. The point of saturation is shown at the intersection of modes 1 and 2 at 10 grams where 100% of the phase change mass melts and freezes, but the temperature never falls below the melting point of 10° C (full freeze occurs at the transition from eclipse to sunlight). Addition of mass beyond this exhibits no additional utilization of latent heat storage, just contributions to sensible heat storage. In fact, as PCM mass is increased in this regime, the increased level of sensible heat storage at temperatures above the melting point lengthen the sensible heat time constant, delaying the start of freezing and further reducing latent heat capacity utilization. Therefore, as PCM mass is added during this regime, the percentage of PCM mass that is frozen decreases. Due to the single-node assumption, the lower temperature in mode 2 is constrained to the melting point. The corresponding hot-side extreme temperature is weakly influenced.

The point at which the maximum frozen PCM mass fraction per orbit reaches zero is represented at the intersection of modes 2 and 4 (yellow and red) where the minimum temperature equal to the melting point is just reached right at the transition

from eclipse to sunlight, but without time for any freezing to occur. Addition of PCM mass beyond this point contributes only to sensible heat capacity above the melting point. Non-utilization of the latent heat capacity in this case yields a mass-inefficient use of the PCM.

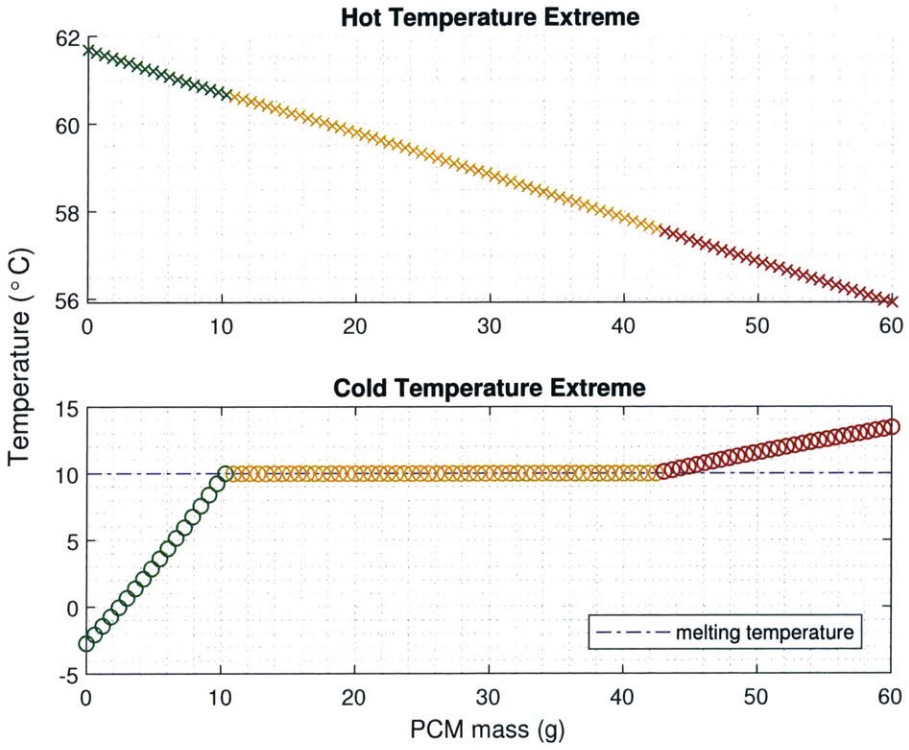

Figure 4-4: Hot and Cold Temperature Extremes vs. PCM mass

4.2 Cold Bias Relative to Transition Temperature

The corresponding cold bias case, draws direct analogies to the hot bias case. However, the internal energy parameter is reduced and the net radiating emissivity is increased to create the cold bias relative to the melting point of the pentadecane at 10° C. Though artificially adjusted in this example, this represents the selection of a PCM with a melting point that is high relative to the thermal energy oscillation.

Steady state temperature oscillation is shown for 'low', 'medium', and 'high' PCM masses in Figures 4-5. The modes are identified in the zoom in in Figure 4-6. Mode 1 is similar in operation to the hot-bias mode 1 where full freezing and melting occur during each orbit. Due to the relative proximity to the upper extreme temperature, the net heat flow rate at the melting point is higher during cooling. Thus, the asymmetric affect is stronger during the sunlit portion of the orbit.

Mode 3 occurs when PCM saturation is reached for melting. In this mode, the excess of phase change mass causes only a partial melt, with full freezing each orbit. Finally, mode 5 is again similar to that in the hot bias case, except that the temperature oscillation lies below the melting point.

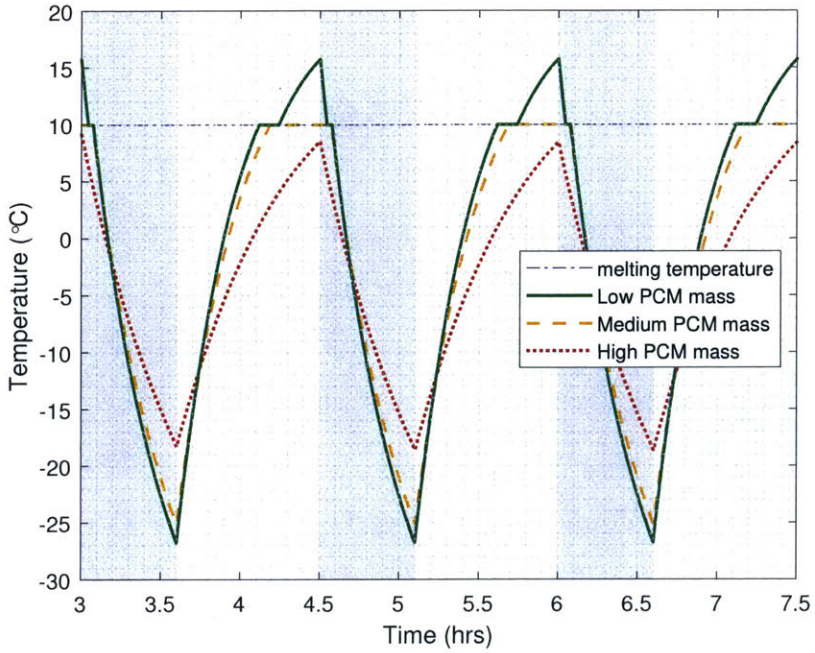

Figure 4-5: Cold-Biased Quasi-Steady State Temperature Oscillation for 3 PCM masses

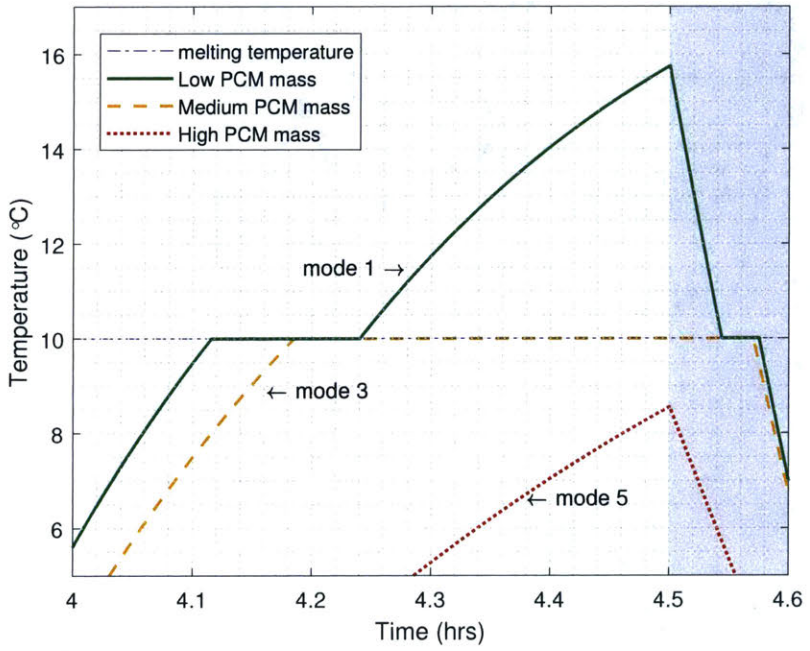

Figure 4-6: Zoom in of figure 4-2 PCM Operation

4.3 Neutral Oscillation About Transition Temperature

The previous two bias cases refer to a mismatch in the PCM melting point and the center of temperature (or thermal energy) oscillation. The asymmetry identified, yields a correspondingly asymmetric effect on the hot and cold extremes. When the PCM melting point and center of temperature oscillation coincide, however, hot and cold extremes are both influenced evenly, eliminating the case where saturation occurs only during either the freezing or melting process. As such, in this case, there exist only two modes: mode 1, full melting and freezing per cycle, and a new mode, mode 6, wherein the temperature is held at a constant for all time.

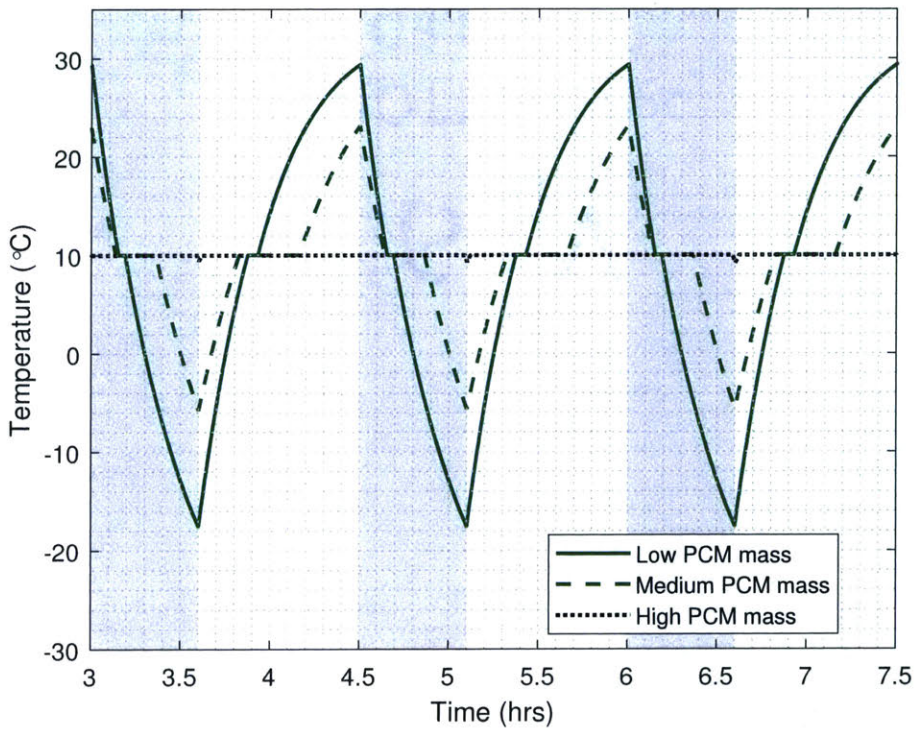

Figure 4-7: Neutral Quasi-Steady State Temperature Oscillation for 3 PCM masses

Temperature oscillation for three PCM masses are displayed in Figure 4-7. In the low and medium PCM mass cases, depicted in green (solid and dashed), the hot and cold temperature extremes are relatively equally affected (it is balanced in energy oscillation, not temperature). For the low and medium mass cases, the PCM fully melts and fully freezes; this is mode 1. As more phase change material is added, the hot and cold extremes both continue to lessen in magnitude. The saturation point, depicted in dotted black, occurs when both the hot and cold extremes reach the melting point; saturation point occurs for melting and freezing simultaneously. Additional mass beyond this has no impact on temperature, which remains unchanged at the melting point.

Additional mass does however, add to margin. Should any parameters such as internal heat, or rates of radiation change momentarily, additional mass beyond the saturation point will allow for extra energy absorption in the latent heat regime. If the balance in energy oscillation changes permanently, the center of thermal energy oscillation will shift and the temperature oscillation may 'fall out' of the latent heat zone; it is an unstable equilibrium.

The variation in hot and cold temperature extremes is shown in Figure 4-8. As mass is increased, both hot and cold extremes are reduced in magnitude until the saturation point, at 81 grams, the start of mode 6. Beyond this point, the temperature is static.

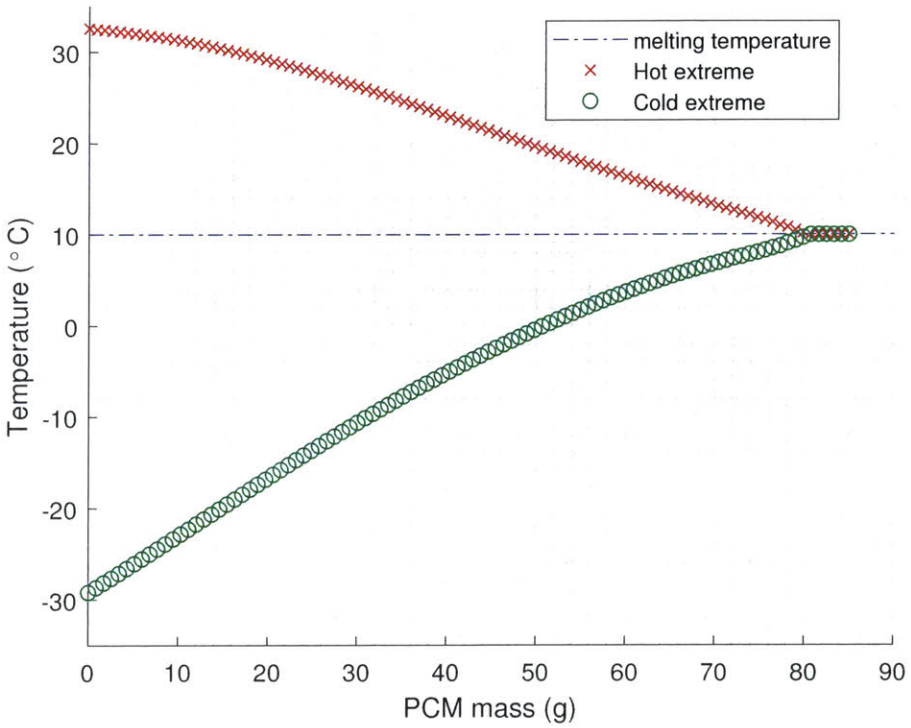

Figure 4-8: Hot and Cold Temperature Extremes vs. PCM mass

4.4 Conclusion

In this chapter, six distinct PCM operating modes are explored through a simplified example. These modes are driven by the relative position of the center of thermal energy oscillation relative to the transition point of the PCM. A mismatch creates a bias – either hot or cold. Both bias cases contain three modes of operation. In mode 1, all of the phase change material freezes and melts during quasi-steady state thermal oscillation. In this mode, all of the latent heat capacity of the PCM is utilized. Increases to the mass of PCM in mode 1 increase the latent heat storage until the point of saturation, where the phase transition is no longer complete during each cycle. In the hot bias case, there is a full liquid transition, but only partial solid phase transition. In the cold bias case, there is a full solid phase transition, but only partial liquid transition. In these two modes – modes 2 and 3 respectively – additional

PCM mass contributes to usable sensible heat capacity, but not to utilizable latent heat capacity. Moreover, as more sensible heat storage is added, the percentage of PCM mass that transitions reduces. When the transition percentage per orbit reaches zero, the PCM enters an operating mode where it remains in a single phase for all time (liquid in the hot bias case, solid in the cold bias case). No latent heat capacity is utilized, only sensible heat storage.

In the two bias regimes, there is an asymmetric effect on the hot and cold temperature extremes. In the hot bias regime, the thermal gradient is lower during the cooling process (eclipse). Therefore, there is a correspondingly longer time delay during the freezing process than melting. As latent heat storage is added, the lower temperature extreme is reduced until it reaches the phase transition point. This behavior is mirrored in the cold bias regime where the melting phase is longer relative to the freezing process, asymmetrically affecting the upper temperature extreme more than the lower extreme.

Asymmetric behavior of PCM operation can be utilized through selection of PCM (specifically by melting temperature). In conditions where one temperature constraint is more constraining than the other, it is more desirable to select a PCM that asymmetrically affects the more constraining temperature extreme. Therefore, there is a coupling of the PCM selection and the range of thermal oscillation relative to the temperature constraints. In the case where one temperature limit is more constraining, a lower mass PCM solution can be identified through selection to more strongly influence that particular limit in quasi-steady state.

The neutral case represents a special set of modes where the center of thermal oscillation and the melting point coincide. Upper and lower temperature extremes are equally affected as more and more PCM mass is added. Therefore, as PCM is added, the saturation point occurs where the PCM neither fully melts nor fully freezes in quasi-steady state. Addition of PCM mass beyond this point yields a constant temperature for all time; the thermal energy oscillates within the partial

phase transition region. Such a regime of operation could be useful in the case where the upper and lower temperature constraints are equally tight. Therefore, an equal impact on the effect of heating and cooling time constants is desired.

Chapter 5

Results

5.1 WaferSat Constants and Fixed Parameters

To assist in defining the cases for analysis, several assumptions about WaferSat are defined. The physical constants for a 400 km altitude are given in Table 5.1 [3] and the fixed parameters for WaferSat are shown in Table 5.2. Although a full parts list for WaferSat is not yet fully known, the anticipated element that will be operationally thermally constraining is the battery. Literature values of battery charging and discharging performance with temperature suggest an acceptable range as shown in Table 5.2 [36, 37].

Table 5.1: Physical Constants

Constant	**Value**
Solar irradiance flux density, E_{sol}	$1367\,\mathrm{W\,m^{-2}}$
Mean Earth Albedo, A_E	0.31
Mean Earth IR flux density	$239\,\mathrm{W\,m^{-2}}$
Temperature of free space, T_{space}	$2.7\,\mathrm{K}$

Table 5.2: WaferSat Fixed Parameters

Fixed Parameter	**Value**
Solar array absorptivity, α_{SA}	0.74 [38]
Solar array emissivity, ε_{SA}	0.85 [39]
Solar array reflectivity, R_{Ω}	0.04
Solar array efficiency, η_{SA}	25%
Wafer area, A_{waf}	$3.14 \times 10^{-2}\,\mathrm{m}^2$
Orbit altitude, h	400 km
Base wafer mass, m_{waf}	236 g

5.1.1 Objective and Constraints

For the following cases, the design objective is to minimize the required PCM mass to meet the following constraints. Wafer absorptivity and emissivity ranges are bounded between 0.1 and 0.9 in equations 5.1 to 5.4.

$$0.1 \leqslant \alpha_T \leqslant 0.9 \tag{5.1}$$

$$0.1 \leqslant \alpha_B \leqslant 0.9 \tag{5.2}$$

$$0.1 \leqslant \varepsilon_T \leqslant 0.9 \tag{5.3}$$

$$0.1 \leqslant \varepsilon_B \leqslant 0.9 \tag{5.4}$$

The internal heat dissipation parameter, Q_{int} is expressed with an equality condition, setting an upper bound on a potential payload power dissipation:

$$Q_{int} = 5.0W \tag{5.5}$$

The per-orbit energy generation from the solar arrays must be greater than or equal to the per-orbit energy dissipation. The per-orbit energy generation is a function of ϕ_{SA}, and the Sun-wafer top projection term, f_{S-T}. The solar array physical fill factor, ϕ_{SA} is also bounded.

$$\int_{t_{s0}}^{t_{sf}} A_{waf}\phi_{SA}f_{S-T}E_{sol}\eta_{SA}dt \geqslant Q_{int}P_{orbit} \tag{5.6}$$

$$0 \leq \phi_{SA} \leqslant 1 \tag{5.7}$$

The hot and cold temperature extremes are limited to the estimated operational ranges of the batteries.

$$\max\left(T_{waf}\right) \leqslant T_{limH} = 45°C \tag{5.8}$$

$$\min\left(T_{waf}\right) \geqslant T_{limC} = 0°C \tag{5.9}$$

Where the temperature extremes are the maximum and minimums attained during quasi-steady state oscillation in the solutions to the time-variant differential equation 3.4.

$$\frac{d}{dt}(mCpT_{waf}) = Q_S - Q_{radT} - Q_{radB} \tag{3.4 revisited}$$

For the initial sun-facing scenario of section 5.2.1, the attitude parameter, γ is constrained to 0 for all time.

$$\bar{\gamma} = 0 \tag{5.10}$$

5.2 Results

5.2.1 Sun-Facing Orbit - Minimum PCM Mass

As shown in the example in chapter 4, the location of the melting point with respect to the center of heat oscillation in quasi-steady state oscillation has a strong impact on the relative impact on the hot and cold temperature extremes. The following evaluation considers a list of paraffins ranging from methane (1 carbon atom, melting point: 90 K) to Heptatriacontane (37 carbon atoms, melting point: 350 K) to encompass the potential range of temperature oscillations. A full list of the 42 considered PCMs and their properties is shown in Appendix A.

In this section, the minimum PCM mass solution for an always sun-facing orbit is presented (recall Figure 3-4). This scenario represents a hot-case as the solar irradiance exposure is maximized. The results for the continuous variables are shown below in Table 5.3.

Table 5.3: Sun-Facing Orbit Continuous Parameters

Parameter	**Value**
wafer top absorptivity, α_T	0.1
wafer top emissivity, ε_T	0.9
wafer bottom absorptivity, α_B	0.1
wafer bottom emissivity, ε_T	0.9
solar array physical fill factor, ϕ_{SA}	0.72

Due to the high heat flux in and maximized solar irradiance, the wafer properties as determined in the inner fmincon loop, go to their limits in order to limit absorbed

visible light (through solar irradiance and Earth albedo), and maximize emitted thermal energy in the IR. To achieve these values, special coatings on the exposed wafer surfaces would be required. As a second effect, the wafer also absorbs a maximum amount of infrared energy due to Earth emitted IR when a wafer surface is Earth-facing. However, the integrated impact of the view factors over the orbit create a net radiative effect to free space. Therefore, the result of the inner loop determination of the continuous variables minimizes net absorbed visible light heat and maximizes net emitted IR heat, aiding in a reduction of the need to store heat in PCM to satisfy the hot condition.

Plots of the searched phase change materials and masses are shown in Figures 5-1 and 5-2 below. Each color represents a different PCM (correlated between the two plots; a solution must select a single PCM and mass that meets both the hot and cold constraint). The red dashed lines indicate the hot and cold temperature bounds. The markers outside of the temperature bounds (above on the T_{hot} plot or below on the T_{cold} plot) are infeasible solutions as they do not meet the temperature constraints. Note also that the effect of the addition of PCM mass with melting points that are outside of the oscillating temperature range are visible in the clustered band of points near the top of Figure 5-1 and the bottom of Figure 5-2. These points are those where the PCM only contributes to sensible heat storage – mode 6 – since the melting point is never crossed. Due to the high internal heat dissipation and Sun-facing attitude, the hot condition is more constraining. The solution, represented by the enlarged green dot, reflects the hot condition constraint, that drives the selection of the minimum PCM mass to satisfy the upper bound temperature. The lower temperature constraint is slack; far above the constraint.

The minimum-mass solution vector of discrete parameters, x_D^*, are summarized

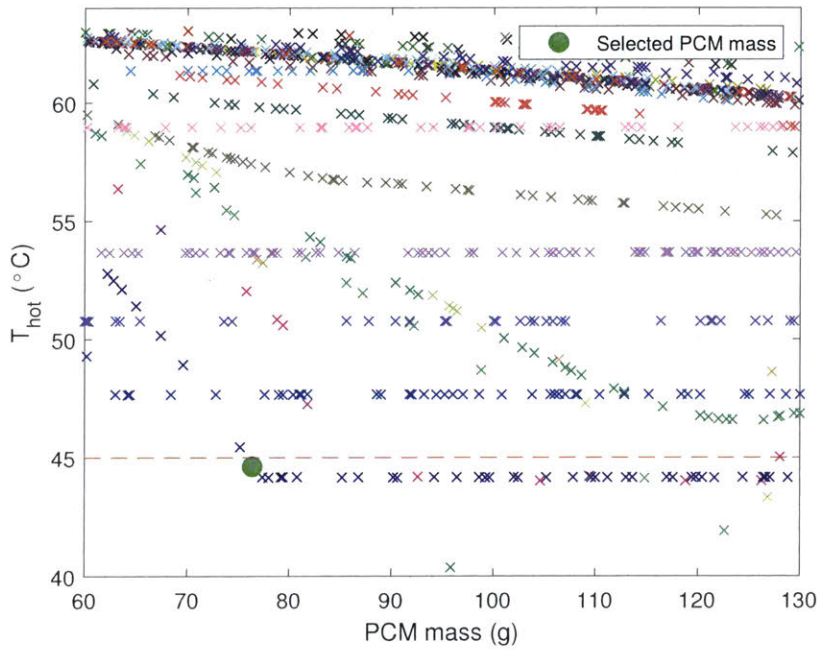

Figure 5-1: Quasi-Steady State Maximum Temperatures vs. PCM mass

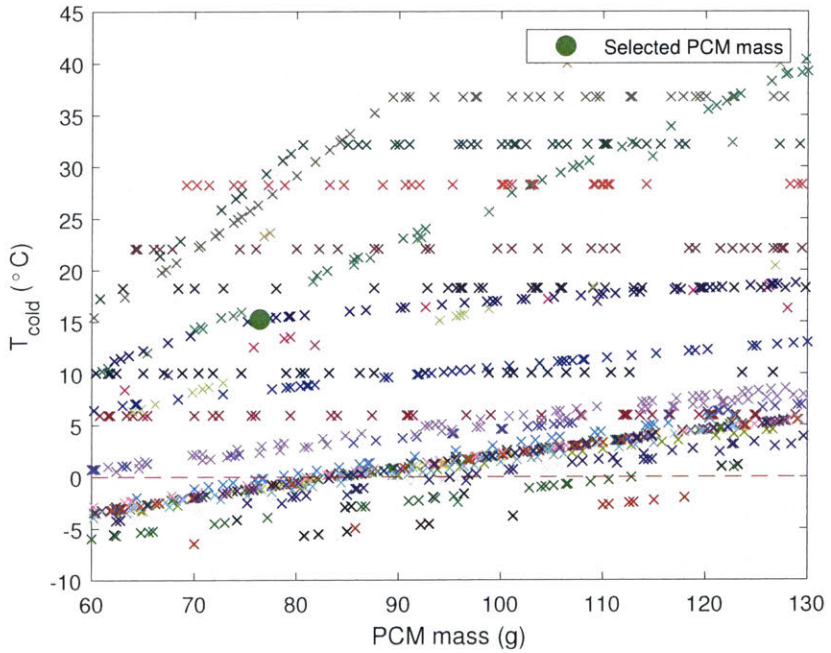

Figure 5-2: Quasi-Steady State Minimum Temperatures vs. PCM mass

in Table 5.4 below. The selected phase change material is Docosane, with a melting point of 44.48° C, just below the upper temperature bound of 45.0° C. The required mass is 76.6 grams.

Table 5.4: Sun-Facing Orbit Discrete Parameters

Parameter	**Value**
Phase change material	Docosane
Melting point	44.15° C
PCM mass	76.6 g
maximum temperature, T_{min}	44.60° C
minimum temperature, T_{max}	15.28° C
Latent heat of fusion, H_m°	$252\,\mathrm{J\,g^{-1}}$
Specific heat capacity, C_p	$2.38\,\mathrm{J\,g^{-1}\,K^{-1}}$
Density	$0.79\,\mathrm{g\,cm^{-3}}$
Chemical formula	$CH_3(CH_2)_{20}CH_3$

Contour plots of the PCM melting point and mass are shown for the quasi-steady state maximum and minimum temperatures in Figures 5-3 and 5-4 respectively. On the maximum temperature side, the selected PCM and mass, indicated by the diamond, are near the left edge of a maximum temperature contour, indicating that it is near the minimum mass condition for the melting point. As a note, the selected point is not exactly at the left edge due to the discretization of the space. Melting points are constrained to real values; subject to gaps in the melting points when selecting another paraffin with one more carbon atom. Additionally, the PCM masses are also discretely selected. Continuous sampling of both parameters would theoretically yield a selected point on the minimum mass edge of this contour.

In contrast, in Figure 5-4, the selected melting point and mass, indicated by the diamond, is not near the edge of a minimum temperature contour. The PCM selection

and mass must be the same in the hot and cold cases, therefore the more constraining of the two conditions determines the outcome, and the other constraint is satisfied with margin.

The temperature oscillation in time can be observed in Figure 5-5. The shaded regions represent eclipse times. The relatively long constant-temperature melting process compared to the shorter delay during eclipse can be observed in the zoom-in near one temperature maximum in Figure 5-6. There is a short period of temperature increase that lasts 21 seconds at the end of each sunlit period, raising the temperature to 44.60° C. The PCM mass is just below the saturation mass.

The maximum temperature in steady-state oscillation of 44.60° C, is slightly higher than the melting point of 44.15° C, indicating that the PCM mass is below saturation point; all of the PCM mass is fully melted and fully frozen in the course of an orbit. This operation corresponds to the cold-biased mode 1 as described in chapter 4 wherein the temperature center of heat oscillation lies below the selected PCM melting point. The asymmetry can also be viewed in Figure 5-6, where the constant temperature periods during eclipse and sunlit portion of the orbit are shown in greater detail. The selection of the melting point nearer to the upper temperature constraint reduces the net heat flow rate during melting of the PCM to lengthen this phase transition, thereby controlling the upper temperature extreme. The heating phase temperature pause (melting process) has a duration of 34 minutes and 38 seconds compared to the 18 minutes and 34 seconds during the cooling phase (freezing process).

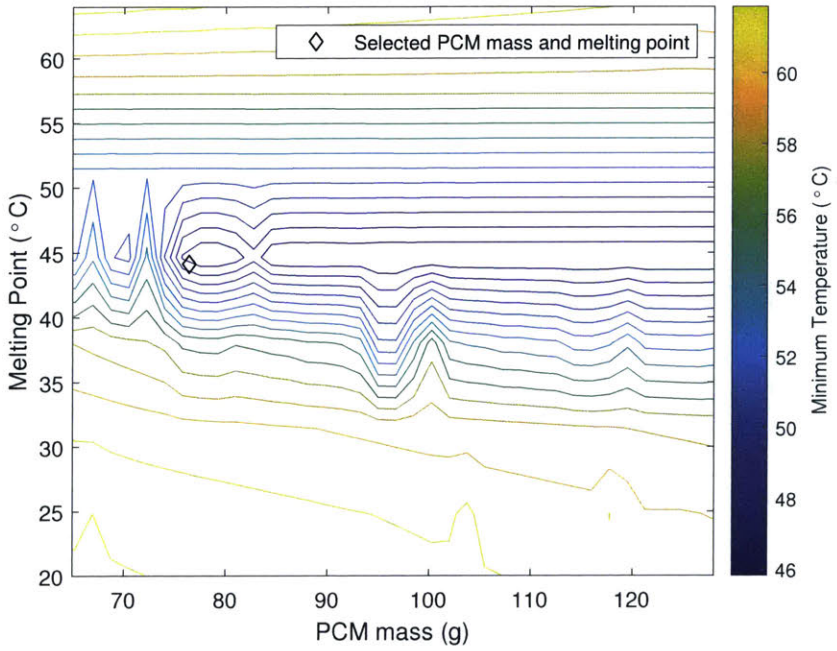

Figure 5-3: Contour of Maximum Temperatures vs. PCM mass and Melting Point

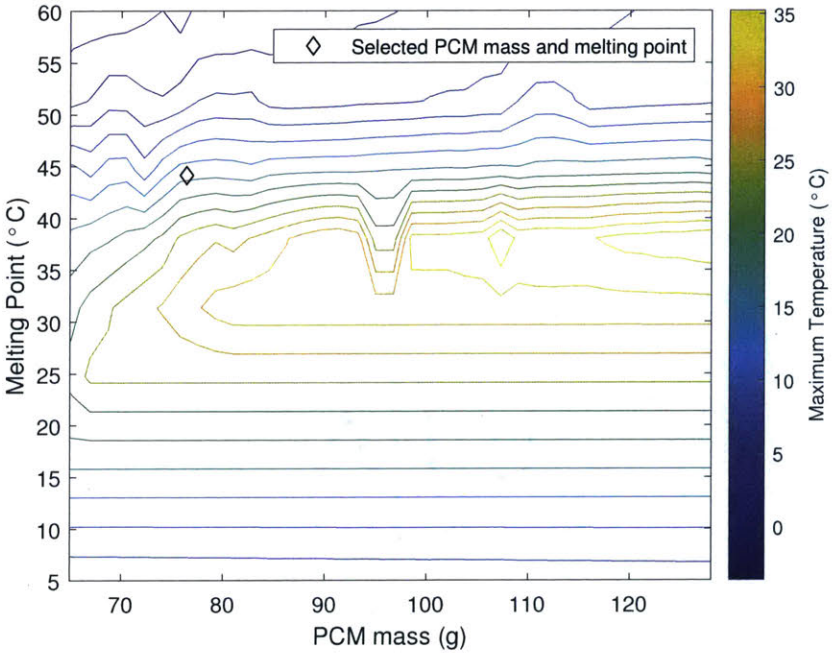

Figure 5-4: Contour of Minimum Temperatures vs. PCM mass and Melting Point

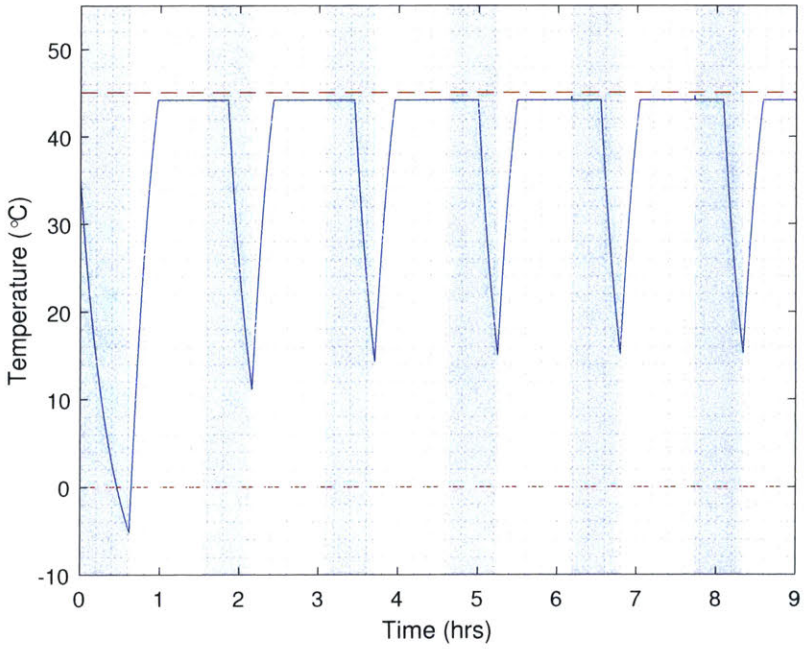

Figure 5-5: Sun-Facing Quasi-Steady State Temperature Oscillation vs. Time

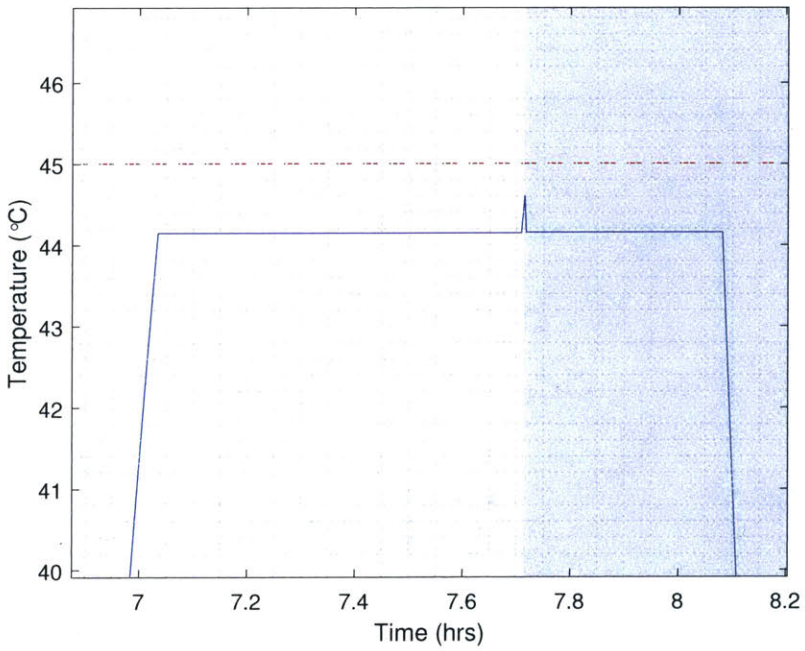

Figure 5-6: Zoom of Maximum Temperature of Sun-Facing Quasi-Steady State Temperature Oscillation vs. Time

5.2.2 Attitude Variation

Recall from section 3.3.4, that the effectiveness of the PCM mass is in the length of the temperature heating/cooling delay. The period of constant temperature effectively increases the time constant, eliciting the behavior of a system with greater thermal inertia over the eclipse and sunlit portions. The length of this temperature heating/cooling delay time is governed by the net heat flow rate, Q_{net} during the phase transition. In a strictly static case, the net heat flow rate term is only a function of temperature and is therefore only modified by the melting point of the PCM.

However, if additional degrees of freedom, such as varied attitude decisions, are introduced to the problem, then Q_{net} can be described as a function of these decisions in time (position in the orbit) as well as temperature. As shown in section 5.2.1, selection of a PCM that is nearest to the lowest net heat flow rate allows for a minimum-mass solution. Manipulation of Wafer attitudes allows for further reduction of the heat flows during transition to select an even lower mass solution. The new solution comes at the expense of a new operational constraint: the specified attitude profile that creates the solution must be followed (and deviation would require margin to consume).

Recall the following equations from section 3.3.4, the freezing case:

$$m_{PCM} H_m^\circ L_{frac} = \int_{t_{p0}}^{t_{p1}} Q_{net}^f(t, T_m) dt \qquad \text{(3.20 revisited)}$$

The melting case:

$$m_{PCM} H_m^\circ (1 - L_{frac}) = \int_{t_{p0}}^{t_{p1}} Q_{net}^m(t, T_m) dt \qquad \text{(3.21 revisited)}$$

where the length of temperature pause in both cases is expressed as:

$$t_{Tpause} = t_{p1} - t_{p0} \qquad \text{(3.22 revisited)}$$

The net heat flow rates during freezing and melting, Q^f_{net} and Q^m_{net} respectively, are now functions in time due to changing view factors to heat sources and to free space as influenced by the attitude decisions in time. A series of discrete attitude decisions for γ, the planar angle to the Earth-Sun vector are now design parameters that can be varied to alter Q_{net}.

The attitude decision γ is discretized into 6 evenly-spaced subdivisions of the orbit, beginning at the start of eclipse. These positions are shown approximately in Figure 5-7. Each element of the vector $\bar{\gamma}$, is an additional parameter to be sampled in the simulated annealing loop. This case seeks to select an overall minimum PCM mass solution that combines melting point selection with control over Q_{net} through radiative view factors and heat source projection terms to create a more effective per-gram time constant impact.

The attitude decisions are subject to the power generation constraint, therefore the attitude decision parameter is constrained to a set of angles. The new constraint is a relaxation of the previous equality constraint setting $\bar{\gamma}$ to zero (equation 5.10, section 5.1.1). At each attitude decision location, the search for γ is constrained to an angle between -0.7 rad and 0.7 rad as shown in equation 5.11. These bounds represent the limiting power generating condition – if all angles are chosen at the limit of ± 0.7 rad, the solar array physical fill factor, ϕ_{SA} is at its limit of 100%. Searching over

angles beyond this limit yield potentially infeasible solutions.

$$-0.7\,\text{rad} \leqslant \bar{\gamma} \leqslant 0.7\,\text{rad} \tag{5.11}$$

The results for the continuous design parameters, discrete design parameters, and $\bar{\gamma}$ are shown in Tables 5.5, 5.6, and 5.7 respectively.

Table 5.5: Attitude Decision Continuous Parameters

Parameter	**Value**
wafer top absorptivity, α_T	0.1
wafer top emissivity, ε_T	0.9
wafer bottom absorptivity, α_B	0.1
wafer bottom emissivity, ε_T	0.71
solar array physical fill factor, ϕ_{SA}	0.79

Table 5.6: Attitude Decision Discrete Parameters

Parameter	**Value**
Phase change material	8-Pentadecanone
Melting point	43.0° C
PCM mass	63.4 g
maximum temperature, T_{min}	44.78° C
minimum temperature, T_{max}	11.37° C
Latent heat of fusion, ΔH_m°	$259\,\text{J}\,\text{g}^{-1}$
Chemical formula	$C_{15}H_{30}O$

The introduction of attitude variation in the design vector changes the selected PCM and significantly reduces the required PCM mass from 76.6 grams to 63.4 grams. Note the change from Docosane to 8-Pentadecanone, with a slightly lower melting

point. In contrast to the Sun-facing case where PCM melting point was selected for a fixed Q_{net}, PCM selection is in combination with adjusted Q_{net}. The result is a selection of a PCM and mass with lower total latent heat capacity than in the Sun-facing case that still meets the thermal requirements.

Table 5.7: Attitude Decision Angles

Position	**True Anomaly, θ**	**Wafer Attitude, γ**
1	139.8°	−31.2°
2	199.8°	−22.3°
3	259.8°	−40.1°
4	319.8°	−13.4°
5	19.8°	−40.1°
6	79.8°	40.1°

Note also in Table 5.5 that the selected wafer bottom emissivity is lower and there is a tendency in the sunlit portions of the orbit (second half of position 3, positions 4, 5, 6) to point the wafer bottom to Earth and the Wafer top (the higher effective absorptivity and emissivity surface) away from Earth, as depicted in Figure 5-7. It can also be observed that the lower γ angles are typically avoided, reducing solar absorption on the high absorptivity side (solar array area).

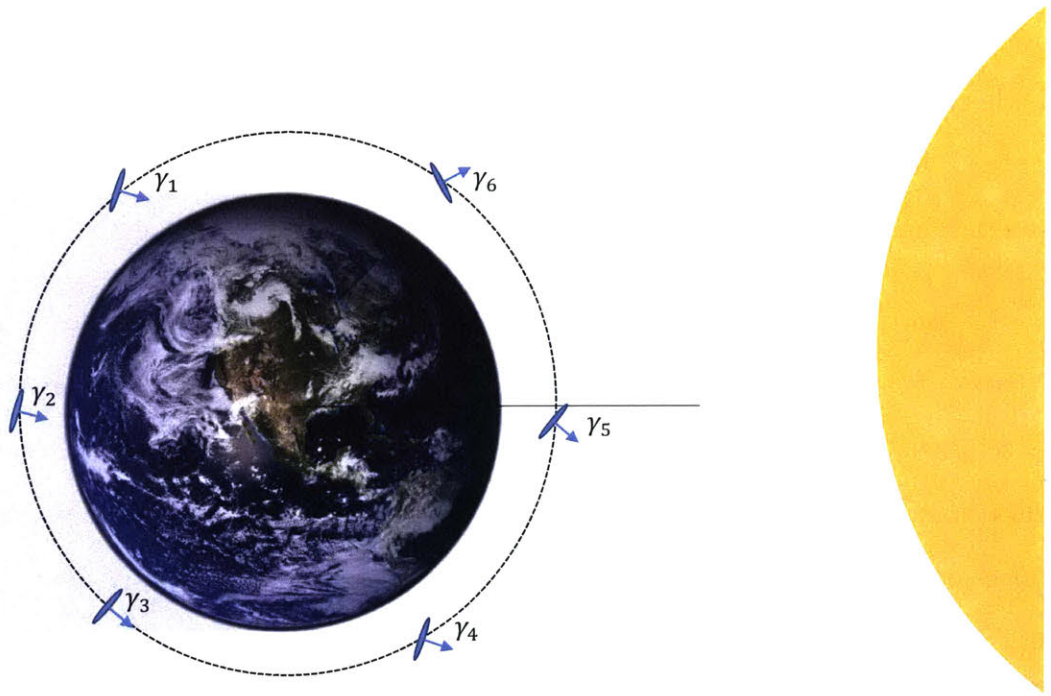

Figure 5-7: Approximate Depiction of Attitude Decisions

5.3 Design Implications

In this chapter, the results of a minimum PCM mass solution are presented for two cases: a fixed-attitude Sun-facing scenario and a constrained, attitude decision scenario. In the Sun-facing case, the selection of PCM melting point is determined by the fixed variation of Q^f_{net} and Q^m_{net} throughout the orbit. Due to the desire to operate with high levels of internal heat dissipation (as an abstraction for increased payload capability or operation), the hot temperature constraint is tight. PCM selection is therefore driven largely by melting point to maximize the duration of the melting process to stretch the heating time constant. The effect is a 'clipping' the hot extreme temperature peaks.

In contrast, when additional degrees of freedom – such as attitude decisions in time – are added to influence the net heat flow rates during phase transition, the effect is to further lengthen the periods of constant temperature (phase transition). Additionally, the PCM melting point is no longer driven by a fixed profile; PCM selection is now made in concert with the attitude decisions that alter the Q_{net} profile in time.

The main impact of PCM mass is to increase thermal heating/cooling time constants to allow for an increase in the internally dissipated heat for a given set of temperature range requirements (that would otherwise cause a violation). PCM mass can be minimized for a fully defined attitude profile, or PCM mass can be globally minimized through PCM selection with identification of a thermally favorable attitude profile. This result implies an inverse problem where the net cost of deviation from the thermally favorable attitude profile is enumerated, allowing for the design of operational modes that minimize PCM mass for a given level of attitude pointing freedom. Therefore, in such a case, the effects of PCM heat storage are to increase

internal heat dissipating ability while allowing for a minimum PCM purchase of selective pointing for operations.

WaferSat is envisioned as a low-mass, flat-profile PicoSat bus. Therefore, feasibility for implementation of PCMs on WaferSat will depend on the mass added and the occupied volume. The minimum PCM masses for the sun-facing and attitude decision scenarios were 76.6 grams and 63.4 grams respectively. If the PCM is incorporated as a thin layer of the same area as the silicon wafer, the thickness, τ_{PCM}, is expressed in equation 5.12. This represents a lower bound on the thickness; encapsulation and other wafer area and internal volume usage may increase the thickness.

$$\tau_{PCM} = \frac{m_{PCM}}{\rho_{PCM} A_{waf}} \tag{5.12}$$

The thickness of the sun-facing solution is 3.1 mm and the thickness of the varied-attitude solution is 2.6 mm. While the magnitudes of the values are low, both solutions add considerable mass and thickness on the scale of a single silicon wafer system. Variation of attitude is able to reduce the required PCM mass through alteration of view factors and heat flow rates. Exploration of other solutions to use in concert with PCMs is needed to further reduce the required mass and volume.

Chapter 6

Conclusion

6.1 Thesis Summary

WaferSat simultaneously presents great potential and many design challenges due to its small size. With low mass and thus low thermal heat storage capacity, phase change materials present a potential option for increasing thermal inertia to prevent equilibration at extreme temperatures beyond operational and survivable levels. The addition of high-density latent heat storage allows for greater efficiency of thermal storage capacity increase than through sensible heat storage alone (increase in base Silicon substrate mass).

This work explores mass-optimal selection of phase change materials in both a prescribed, fixed attitude scenario and in a constrained, non-fixed attitude scenario. It was found that the addition of the degrees of freedom afforded by the discrete attitude decisions allows for a new combined PCM selection result and lower required PCM mass.

Results suggest that PCM mass could potentially be utilized to both increase

power dissipating capability within thermal requirements and allow for selective pointing. Further exploration of the marginal cost of selective attitude freedom can aid in operational design of missions that maximally utilize the benefits of increased heat storage on a very small satellite platform. However, consideration of mass and volume implementation on a single silicon wafer suggests that more exploration to reduce the required PCM mass is needed.

6.2 Thesis Contributions

Contributions of this work are summarized below:

- An integrated approach towards satisfaction of thermal temperature ranges using PCM mass in the presence of other subsystem constraints is presented.

- Modes of PCM heat storage operation are identified. Mass efficiency of modes and periods of heat storage are explored through a simplified example. The operational modes are identified in the results.

- A minimum PCM mass solution for a Sun-facing attitude scenario is presented. PCM properties are selected based on net heat flows and heating time constant increase.

- A minimum PCM mass and thermally-favorable attitude profile is identified. Co-variation of net heat flows in time, through thermal view factor alteration yields a different PCM selection and lower mass solution. Although this PCM and mass have a lower total latent heat storage, the net increase in heating time constant satisfies constraints and meets thermal requirements at a lower mass impact.

- The ability of PCM latent heat storage to increase the thermal time constant of a low mass system is demonstrated. However, more design variable exploration is needed to further increase PCM mass efficiency and increase feasibility at-scale.

6.3 Future Work

Avenues for expansion upon this work include:

- Discretization of attitudes is coarse in this work. Finer discretization combined with efficient, conflict-directed methods [40] may allow for greater detail in selection of both thermally favorable attitude profiles and cases with selective pointing. Such resolution may reveal non-unique solutions that allow for co-variation of attitudes at different locations in an orbit to achieve a result.

- Quantification of the sensitivity of PCM mass growth as functions of orbital position and attitude are needed to approach the inverse problem to design excess latent heat storage to 'purchase' selective pointing. This may be achieved in combination with the previous item using conflict-directed search.

- Considerations of quasi-static equilibrium beyond single orbits may allow for other modes of operation. Multi-orbit periods may allow for duty cycled operation that exploits the relative slackness of the cold temperature extreme constraint. A number of orbits of net cooling may allow for increased heat dissipation over short periods.

- Quantification of the PCM mass cost of margin may also allow for varied orbit scenarios beyond strict single-orbit quasi-static equilibrium.

- Additional degrees of freedom such as electrochromic [41, 42] control of surface

thermal properties may increase control over Q_{net} to further reduce required PCM mass and allow for selective pointing at lower PCM cost.

Appendix A

List of PCMs

Table A.1: PCM List

Material	**C atoms**	**Molar mass**	T_{melt}	H_m°	C_p	**Density**
		$g\ mol^{-1}$	K	$J\ g^{-1}$	$J\ g^{-1}\ K^{-1}$	$g\ cm^{-3}$
Methane	1	16	90.68	58	2.24	0.658
Ethane	2	30	90.38	95	1.19	1.240
Propane	3	44	85.47	80	1.27	1.834
Butane	4	58	134.79	105	1.32	2.455
Pentane	5	72	143.45	117	1.67	0.621
Hexane	6	86	177.83	152	2.27	0.655
Heptane	7	100	182.55	141	2.25	0.649
Octane	8	114	216.37	181	2.23	0.699
Nonane	9	128	219.65	170	1.64	0.714
Decane	10	142	243.5	202	2.1	0.726
Undecane	11	156	247.55	177	2.19	0.737
Dodecane	12	170	263.55	216	2.21	0.745

Material	**C atoms**	**Molar mass**	T_{melt}	H_m°	C_p	**Density**
		$g\ mol^{-1}$	K	$J\ g^{-1}$	$J\ g^{-1}\ K^{-1}$	$g\ cm^{-3}$
Tridecane	13	184	267.75	196	2.22	0.753
Tetradecane	14	198	278.95	227	2.19	0.759
Pentadecane	15	212	283.05	207	2.21	0.765
Hexadecane	16	226	291.25	236	2.19	0.77
Heptadecane	17	240	295.05	214	2.18	0.775
Octadecane	18	254	301.25	244	2.24	0.779
Nonadecane	19	268	305.15	222	2.25	0.782
Heneicosane	21	296	313.35	213	2.25	0.788
Docosane	22	310	317.15	252	2.38	0.791
Tricosane	23	324	320.65	234	2.38	0.793
Tetracosane	24	338	323.75	255	1.78	0.796
Pentacosane	25	352	326.65	238	2.32	0.798
Hexacosane	26	352	326.65	250	2.47	0.8
Heptacosane	27	380	331.95	235	2.18	0.802
Octacosane	28	394	334.35	254	2.38	0.803
Nonacosane	29	408	336.35	239	2.2	0.805
Triacontane	30	422	338.55	252	1.92	0.806
Hentriacontane	31	436	341.05	242	2.09	0.808
Dotriacontane	32	450	342.85	266	1.95	0.809
Tritiacontane	33	464	344.55	256	2.2	0.81

Material	**C atoms**	**Molar mass**	T_{melt}	H_m°	C_p	**Density**
		$g\ mol^{-1}$	K	$J\ g^{-1}$	$J\ g^{-1}\ K^{-1}$	$g\ cm^{-3}$
Tetratriacontane	34	478	346.25	268	2.2	0.811
Pentatriacontane	35	492	347.85	257	1.86	0.812
Hexatriacontane	36	506	349.35	269	2.2	0.814
Heptatriacontane	37	520	350.85	259	2.2	0.815
8-Pentadecanone			313	259	2.2	
p-Joluidine			316.3	167	2.2	
Cyanamide			317	209	2.2	
Lauric acid			317.2	211.6	2.2	

Bibliography

[1] Barnhart, D. J., Vladimirova, T., and Sweeting, M. N., "System-on-a-chip design of self-powered wireless sensor nodes for hostile environments," 2007, pp. 1–12.

[2] Manchester, Z., Peck, M., and Filo, A., "Kicksat: A crowd-funded mission to demonstrate the world's smallest spacecraft," 2013.

[3] Larson, W. J. and Wertz, J. R., *Space Mission Analysis and Design*, Microcosm Press, El Segundo, CA, 3rd ed., 1999.

[4] Stouffer, C. J., Hagood, R. M., and Bugby, D. C., "Cryogenic Thermal Storage Unit (CRYOTSU) Flight Experiment," Vol. 2, 1997, pp. 1409–1414.

[5] Lambe, A. B. and Martins, J. R., "Extensions to the design structure matrix for the description of multidisciplinary design, analysis, and optimization processes," *Structural and Multidisciplinary Optimization*, Vol. 46, No. 2, 2012, pp. 273–284.

[6] Du, K., Calautit, J., Wang, Z., Wu, Y., and Liu, H., "A review of the applications of phase change materials in cooling, heating and power generation in different temperature ranges," *Applied Energy*, Vol. 220, 2018, pp. 242–273.

[7] Sun, N. and Xiao, Z., "Paraffin wax-based phase change microencapsulation embedded with silicon nitride nanoparticles for thermal energy storage," *Journal of materials science*, Vol. 51, No. 18, 2016, pp. 8550–8561.

[8] Selva, D. and Krejci, D., "A survey and assessment of the capabilities of Cubesats for Earth observation," *Acta Astronautica*, Vol. 74, 2012, pp. 50–68.

[9] Poghosyan, A. and Golkar, A., "CubeSat evolution: Analyzing CubeSat capabilities for conducting science missions," *Progress in Aerospace Sciences*, Vol. 88, 2017, pp. 59–83.

[10] Heidt, H., Puig-Suari, J., Moore, A., Nakasuka, S., and Twiggs, R., "CubeSat: A new generation of picosatellite for education and industry low-cost space experimentation," 2000.

[11] McNutt, C. J., Vick, R., Whiting, H., and Lyke, J., "Modular Nanosatellites–(Plug-and-Play) PnP CubeSat," 2009.

[12] Joshi, A., J. Keller interview of A. Joshi, February 1994.

[13] Cutler, J. and Hutchins, G., "OPAL: Smaller, Simpler, and Just Plain Luckier," 2000.

[14] Janson, S., "Micro/nanotechnology for micro/nano/picosatellites," 2003, pp. 6269.

[15] Hartzell, A. L. and Woodilla, D. J., "MEMS reliability, characterization, and test," Vol. 4558, 2001, pp. 1–6.

[16] Barnhart, D. J., Vladimirova, T., and Sweeting, M. N., "Satellite-on-a-Chip development for future distributed space missions," 2006, pp. 199–212.

[17] Parkin, K. L., "The breakthrough starshot system model," *Acta Astronautica*, Vol. 152, 2018, pp. 370–384.

[18] Estavez, D., "Detecting the Sprites from KicksSat-2," Available at `https://destevez.net/2019/04/detecting-the-sprites-from-kicksat-2/` (2019/04/19).

[19] Brashears, T., Lubin, P., Rupert, N., Stanton, E., Mehta, A., Knowles, P., and Hughes, G. B., "Building the future of wafersat spacecraft for relativistic spacecraft," Vol. 9981, 2016, pp. 998104.

[20] Barnhart, D. J., Vladimirova, T., and Sweeting, M. N., "Satellite-on-a-Chip: A Feasibility Study," 2006, pp. 199–212.

[21] Stout, K. D., *Design Optimization of Thermal Paths in Spacecraft Systems*, Master's thesis, Massachusetts Institute of Technology, 2013.

[22] Creel, R. A., "Apollo Rover Lessons Learned: Applying Experiences on the Apollo Lunar Rover Project to Rovers for Future Space Exploration," `https://history.nasa.gov/alsj/creel_lrv_experiences_alsj.pdf`, 2007, An optional note.

[23] Pauken, M., Emis, N., Van Luvender, M., Polk, J., and Del Castillo, L., "Thermal control technology developments for a Venus lander," Vol. 1208, No. 1, 2010, pp. 68–75.

[24] Bugby, D. C., Stouffer, C. J., Hagood, R. M., Rich, M., Tomlinson, B., Davis, T. M., Ku, J., and Swanson, T. D., "Development and testing of the CRYOTSU flight experiment," 1998.

[25] Collette, J., Rochus, P., Peyrou-Lauga, R., Pin, O., Nutal, N., Larnicol, M., and Crahay, J., "Phase change material device for spacecraft thermal control," 2011.

[26] Jilla, C. D., Miller, D. W., and Sedwick, R. J., "Application of multidisciplinary design optimization techniques to distributed satellite systems," *Journal of Spacecraft and Rockets*, Vol. 37, No. 4, 2000, pp. 481–490.

[27] Jilla, C. and Miller, D., "A multiobjective, multidisciplinary design optimization methodology for the conceptual design of distributed satellite systems," 2002, pp. 5491.

[28] Jilla, C. D., *A Multiobjective, Multidisciplinary Design Optimization Methodology for the Conceptual Design of Distributed Satellite Systems*, Ph.D. thesis, Cambridge, MA, 2002.

[29] De Weck, O. L. and Jones, M. B., "Isoperformance: Analysis and design of complex systems with desired outcomes," *Systems engineering*, Vol. 9, No. 1, 2006, pp. 45–61.

[30] de Weck, O. L., *Multivariable Isoperformance Methodology for Precision Opto-Mechanical Systems*, Ph.D. thesis, Cambridge, MA, 2001.

[31] Martins, J. R. and Lambe, A. B., "Multidisciplinary design optimization: a survey of architectures," *AIAA journal*, Vol. 51, No. 9, 2013, pp. 2049–2075.

[32] Wang, F., Maidment, G., Missenden, J., and Tozer, R., "The novel use of phase change materials in refrigeration plant. Part 1: Experimental investigation," *Applied Thermal Engineering*, Vol. 27, No. 17-18, 2007, pp. 2893–2901.

[33] Mondieig, D., Rajabalee, F., Laprie, A., Oonk, H. A., Calvet, T., and Cuevas-Diarte, M. A., "Protection of temperature sensitive biomedical products using molecular alloys as phase change material," *Transfusion and apheresis science*, Vol. 28, No. 2, 2003, pp. 143–148.

[34] Waqas, A. and Din, Z. U., "Phase change material (PCM) storage for free cooling of buildings—a review," *Renewable and sustainable energy reviews*, Vol. 18, 2013, pp. 607–625.

[35] Hale, D., Hoover, M., and ONeill, M., "Phase change materials handbook," 1971.

[36] Waldmann, T., Wilka, M., Kasper, M., Fleischhammer, M., and Wohlfahrt-Mehrens, M., "Temperature dependent ageing mechanisms in Lithium-ion batteries–A Post-Mortem study," *Journal of Power Sources*, Vol. 262, 2014, pp. 129–135.

[37] Carter, B., Matsumoto, J., Prater, A., and Smith, D., "Lithium ion battery performance and charge control," Vol. 1, 1996, pp. 363–368.

[38] Santbergen, R. and van Zolingen, R. C., "The absorption factor of crystalline silicon PV cells: A numerical and experimental study," *Solar energy materials and solar cells*, Vol. 92, No. 4, 2008, pp. 432–444.

[39] Riverola, A., Mellor, A., Alvarez, D. A., Llin, L. F., Guarracino, I., Markides, C., Paul, D., Chemisana, D., and Ekins-Daukes, N., "Mid-infrared emissivity of crystalline silicon solar cells," *Solar Energy Materials and Solar Cells*, Vol. 174, 2018, pp. 607–615.

[40] Williams, B. C. and Ragno, R. J., "Conflict-directed A* and its role in model-based embedded systems," *Discrete Applied Mathematics*, Vol. 155, No. 12, 2007, pp. 1562–1595.

[41] Chandrasekhar, P., Zay, B. J., Lawrence, D., Caldwell, E., Sheth, R., Stephan, R., and Cornwell, J., "Variable-emittance infrared electrochromic skins combining unique conducting polymers, ionic liquid electrolytes, microporous polymer membranes, and semiconductor/polymer coatings, for spacecraft thermal control," *Journal of Applied Polymer Science*, Vol. 131, No. 19, 2014.

[42] Demiryont, H., Shannon III, K., and Ponnappan, R., "Electrochromic devices for satellite thermal control," Vol. 813, No. 1, 2006, pp. 64–73.

[43] Sheffield, J. W. and Wen, C., "Phase Change Material for Spacecraft Thermal Management," 1989.

[44] Sharma, A., Tyagi, V. V., Chen, C., and Buddhi, D., "Review on thermal energy storage with phase change materials and applications," *Renewable and Sustainable energy reviews*, Vol. 13, No. 2, 2009, pp. 318–345.

[45] Mulligan, J., Colvin, D., and Bryant, Y., "Microencapsulated phase-change material suspensions for heat transfer in spacecraft thermal systems," *Journal of spacecraft and rockets*, Vol. 33, No. 2, 1996, pp. 278–284.

[46] Pal, D. and Joshi, Y. K., "Thermal management of an avionics module using solid-liquid phase-change materials," *Journal of Thermophysics and Heat Transfer*, Vol. 12, No. 2, 1998, pp. 256–262.

[47] Kim, T. Y., Hyun, B.-S., Lee, J.-J., and Rhee, J., "Numerical study of the spacecraft thermal control hardware combining solid–liquid phase change material and a heat pipe," *Aerospace Science and Technology*, Vol. 27, No. 1, 2013, pp. 10–16.